Master of Science in Aerospace Engineering

Politecnico di Torino

Master Thesis
Academic Year 2023-2024

Indirect optimization of low-thrust collision avoidance trajectories in LEO with bang-bang control laws

Supervisors:
Prof. Manuela Battipede
Dr. Luigi Mascolo

Candidate:
Giacomo Sarcletti

July 2024

Summary

The ever-increasing density of objects in low Earth orbit (LEO) has raised concerns about the potential for a future cascade of collisions, a phenomenon known as the Kessler Syndrome. Such collisions could inflate the amount of space debris, posing significant risks to operational satellites and future space missions. In response to this, and in alignment with new de-orbit regulations, there is a shift towards refining collision avoidance strategies to minimize propellant consumption. Indeed, despite the relatively low fuel requirements of individual collision avoidance maneuvers, their growing necessity places a considerable strain on satellite fuel budgets.

In this context, the objective of this research is to develop a tool that uses indirect optimization to identify propellant-efficient collision avoidance trajectories between two orbiting objects. To this end, the indirect approach is employed to exploit the theory of optimal control, applied to spacecraft trajectories, and to transform the optimization problem into a boundary value problem, which is subsequently solved by means of shooting procedures. This method ensures precise optimization and offers significant advantages in terms of computational costs, particularly when low-thrust is considered.

The study uses a modified version of a collision probability calculation method originally developed by Alfano and Negron. This method assesses the risk of collision between two objects in a high-fidelity LEO dynamic model. Meanwhile, trajectory optimization is performed using a simpler two-body dynamic model. This approach ensures robust convergence of the optimization method and maintains dynamic accuracy, due to the low maneuvering times involved.

Moreover, this work offers valuable theoretical insights into the indirect optimization method and illustrative examples that facilitate a more comprehensive grasp of the method's practical implementation.

Acknowledgements

Table of Contents

List of Tables

List of Figures

Chapter 1

Introduction

1.1 Preface

Since the advent of the Space Age, there has been a pronounced emphasis across a range of disciplines associated with space exploration on the development of technical and theoretical solutions aimed at enhancing the payload fraction, even by modest increments. This focus is largely a consequence of the fact that while the payload mass encapsulates the entirety of a mission's objectives, it constitutes merely a fraction of the total spacecraft or launcher mass. In the field of mission analysis, the Tsiolkovsky equation stands as a fundamental tool for comprehending how trajectory optimization can maximize the payload mass:

$$\frac{m_f}{m_i} = \exp{-\frac{\Delta v}{c}} \tag{1.1}$$

The "rocket equation" indicates that the final mass increases when the required delta-v decreases, suggesting that the mass of a mission's payload can be higher if the same mission can be executed with a more efficient flight profile.

Various trajectory optimization approaches have been developed over the years. Derek Lawden's work in 1963 [1] initiated the exploration of space trajectory optimization. His research focused on deriving optimal analytical solutions for simplified space flight missions, utilizing optimal control theory principles.

Optimal control theory, with roots dating back to the 17th century, has seen significant advancements over the years. Contributions from mathematicians like Euler, Bellman, and Pontryagin have paved the way for understanding and solving optimization problems in various domains, including space trajectory planning.

In recent decades, the interest in space trajectory optimization has continued to grow, driven by the increasing complexity of space missions. While the foundational principles remain unchanged, the application of optimization theory has evolved, particularly with the development of numerical optimization methods.

1.2 Research Topic

The issue of space debris in Low Earth Orbit (LEO) is a growing concern within the space community. The term "Kessler Syndrome" refers to a scenario proposed by NASA scientist Donald J. Kessler in 1978, which describes a runaway chain reaction of collisions between objects in space [2]. Essentially, when two objects collide, they create more debris, which increases the likelihood of further collisions, leading to a cascading effect where the amount of debris grows exponentially. This poses significant risks to operational satellites, spacecraft, and future space missions.

Satellites in lower orbits face an increased risk of collision due to the dense presence of defunct satellites, spent rocket stages and other debris. This risk is amplified by the increasing number of large constellations of small satellites occupying these altitudes, resulting in a higher frequency of potential conjunction events. As a result, there is a growing emphasis on developing and implementing effective collision avoidance strategies to reduce the risk of accidental collisions and ensure the sustainability of space operations.

Satellite operators are implementing various collision avoidance techniques to safeguard their spacecrafts. These strategies typically involve monitoring the satellites' orbital path and the surrounding space environment using ground-based radar and space-based sensors. If a potential collision is detected, operators can maneuver the endangered satellite to a safer orbit, either by adjusting its trajectory slightly or by performing a larger orbital maneuver to avoid the debris entirely.

One important consideration in refining collision avoidance strategies is minimizing propellant consumption: although these kind of maneuvres usually require low fuel expenditures, un-optimized maneuvering to avoid debris can deplete limited onboard propellant reserves prematurely, reducing the satellite's operational lifespan.

This work aims to provide a valuable contribution to this field by exploiting the indirect optimization method to identify propellant-efficient collision avoidance trajectories with low-thrust propulsion.

1.3 Dissertation overview

A concise outline of the thesis contents is here provided.

- Chapter 2 presents a brief introduction on the main optimization methods used in spacecraft trajectory optimization and follows with the definition of an optimal control problem, the indirect approach to the problem and the main solving methods utilized. Two theoretical examples illustrate how the described method can be applied.

- Chapter 3 describes the reference systems and the dynamic models involved in this work.

- Chapter 4 illustrates the methodology used to perform close approach analysis and the general workflow implemented to identify elegible collision avoidance maneuvers.

- Chapter 5 provides practical information onto the method's implementation and an orbital transfer optimization example with comments.

- Chapter 6 finally delivers the results of an example conjunction event and subsequent evasion maneuver, along with an in-depth analysis of the solution behavior.

- The closing statements in chapter 7 offer a summary of the most significant achievements of the work and suggest potential future improvements.

Chapter 2

Spacecraft Trajectory Optimization

2.1 Introduction

Trajectory analysis and optimization is crucial to the success or even feasibility of a space mission. The problem can be stated as the determination of a trajectory that satisfies some constraints required by the mission, while extremizing some quantity of importance. Since the trajectory followed by a spacecraft directly impacts on the amount of propellant needed for set mission, hence influences the mass budget, which relates to mission feasibility and costs, the most common objective is to minimize propellant consumption or equivalently to maximize the spacecraft's final mass.

Most of the methods used for the optimization of space trajectories fall into three main categories: direct methods, indirect methods, and evolutionary algorithms. Direct methods discretize trajectory and controls and, starting from a guess solution, evaluate a performance index and constraint satisfaction; with the aim of improving the performance index, this parameter optimization problem is then solved by means of gradient-based procedures. Direct methods provide a straightforward implementation, high robustness and good capability of treating complex problems. However, since the solution is based on the approximation made through dicretization, a dense mesh is required in order to obtain accurate results, hence computational costs are usually high [3]. Indirect methods use the optimal control theory (OCT) to derive first-order necessary conditions and transform the optimization problem into a boundary value problem (BVP), which is then solved, starting from a tentative solution, by means of shooting procedures. The most important feat of indirect methods is that they provide first order optimal solutions -in the limits of the dynamic model and the numerical accuracy of integration-.

Moreover they offer low computational costs and vast theoretical insight over the optimization problem, but the necessity of deriving case-specific equations and defining near-optimal guesses have made these methods less appealing than the direct ones. Further information about the state-of-the-art in numerical methods to solve optimal control problems can be found in [4]. Lastly, evolutionary algorithms are comparatively simple and easy to use, they don't require a tentative solution and offer higher robustness. They make use of populations of solutions that evolve towards the optimum following rules that often mimic natural phenomena. Relying on heuristic methods, the solutions obtained have no proof of being the actual global optima.

The most suitable mathematical formulation for an optimization problem regarding finite-thrust missions is a time-continuous optimal control problem [5]. In section 2.2.1 a general statement of the problem will be provided, followed by a more in-depth description of the optimization method adopted in this work (i.e., the indirect method) starting from section 2.2.2.

2.2 The Optimal Control Problem

An Optimal Control Problem (OCP) aims at maximizing a chosen merit index by establishing an admissible control law, while ensuring that the system satisfies specified constraints, as it evolves from an initial to a final state over a defined time interval.

2.2.1 General Statement

The system is described by a set of state variables $\mathbf{x}(t) \in \mathbb{R}^n$ that evolve over time according to n first order differential equations. These ODEs are function of the state vector $\mathbf{x}(t)$, the control vector $\mathbf{u}(t) \in \mathbb{R}^m$, which contains the m control variables, and, of course, the independent variable time t. The ODE system can be generically written as:

$$\dot{\mathbf{x}}(t) = \boldsymbol{f}(\mathbf{x}(t), \mathbf{u}(t), t) \tag{2.1}$$

An optimal solution defines the optimal trajectory $\mathbf{x}^*(t)$, subject to optimal controls $\mathbf{u}^*(t)$, that maximizes a specified merit index. As previously mentioned, the optimal trajectory has to satisfy constraints of various kind; if these constraints concern state and time solely at the extremes of the time interval, the problem defined in (2.1) is a Two Point Boundary Value Problem (TPBVP) and the extremal boundary conditions imposed at $t = t_0$ and at $t = t_f$ are called external boundaries. These BCs can be written as a set of homogeneous algebraic equations and grouped in the constraint vector:

$$\boldsymbol{\psi}(\mathbf{x}_0, \mathbf{x}_f, t_0, t_f) = \mathbf{0} \tag{2.2}$$

where $\psi : [\mathbb{R}^n, \mathbb{R}^n, \mathbb{R}, \mathbb{R}] \to \mathbb{R}^q$ collects the q constraints; $\mathbf{x}_0$ and $\mathbf{x}_f$ stand for $\mathbf{x}(t_0)$ and $\mathbf{x}(t_f)$ respectively.

Constraints may also concern the control variables $\mathbf{u}$, therefore $\mathbf{u} \in \boldsymbol{U}$, where $\boldsymbol{U}$ represents the set of admissible controls.

The criterion that completes the OCP and drives the optimization process is represented by the merit (or performance) index J, which must be maximized or minimized. In general, J is a functional comprised of two terms:

$$J = \varphi(\mathbf{x}_0, \mathbf{x}_f, t_0, t_f) + \int_{t_0}^{t_f} [\Phi(\mathbf{x}(t), \mathbf{u}(t), t)] \, dt \tag{2.3}$$

- The first function φ depends uniquely on the values assumed by the state and time variables at the boundaries. φ quantifies the cost of reaching the desired final state;

- The second term, being an integral over the time interval, depends on the values that the state variables, controls and time assume during the trajectory. This term quantifies how the solution evolved between the initial and final states.

Equation (2.3) can be equivalently rewritten in Lagrange's or in Mayer's formulation, respectively by posing $\varphi = 0$ or $\Phi = 0$ and by introducing opportune auxiliary variables. Mayer's formulation is usually preferred to define an optimization problem that searches for extremal values of a functional, which is the case of this work's OCP.

The problem described in equations (2.1) to (2.3) is called Bolza Problem. A concise mathematical formulation of this time-continuous optimization problem is here presented, utilizing Mayer's formulation of the merit index:

$$P_{Bolza} = \begin{cases} \max_{u \in U} \quad J = \varphi(\mathbf{x}_0, \mathbf{x}_f, t_0, t_f) \\[2mm] \dot{\mathbf{x}}(t) = \boldsymbol{f}(\mathbf{x}(t), \mathbf{u}(t), t) \\[2mm] s.t. \quad \boldsymbol{\psi}(\mathbf{x}_0, \mathbf{x}_f, t_0, t_f) = \mathbf{0} \end{cases} \tag{2.4}$$

Maximization can be turned to minimization by changing the sign of φ; in this work, a maximization problem will be considered.

2.2.2 Necessary Conditions

A necessary, or first order, condition for optimality dictates that the first variation of the performance index J must be zero for any permissible variation along the trajectory and at the boundaries [6].

A modified functional, or augmented merit index, J^* is defined through the introduction of Lagrange multipliers μ and adjoint variables λ [7]:

- Lagrange multipliers are constants associated with boundary conditions and provide a measure of how much the constraints are respected. They are collected in the q-component vector $\boldsymbol{\mu}$;

- Adjoint variables, also reffered to as *costates*, are linked to the state variables and provide a measure of the weigth of each state variables over the merit index. They are collected in the n-component adjoint vector $\boldsymbol{\lambda}$.

The modified functional in Mayer's formulation is defined as:

$$J^* = \varphi + \boldsymbol{\mu}^T \boldsymbol{\psi} + \int_{t_0}^{t_f} [\boldsymbol{\lambda}^T (\boldsymbol{f} - \dot{\mathbf{x}})] \, dt \tag{2.5}$$

where:

$$\varphi \triangleq \varphi(\mathbf{x}_0, \mathbf{x}_f, t_0, t_f) \tag{2.6a}$$

$$\boldsymbol{\psi} \triangleq \boldsymbol{\psi}(\mathbf{x}_0, \mathbf{x}_f, t_0, t_f) \tag{2.6b}$$

$J^* = J$ if $\boldsymbol{\psi} = 0$ and $\boldsymbol{f} - \dot{\mathbf{x}} = 0$, that is if all boundary conditions and differential equations are respected, therefore, solving the augmented problem with the modified functional in equation (2.5) is mathematically equivalent to solving the problem defined in (2.4), provided all constraints are respected.

A simpler expression for J^* can be obtained by integrating the $-\boldsymbol{\lambda}^T \dot{\mathbf{x}}$ term in equation (2.5) by part:

$$\int_{t_0}^{t_f} (-\boldsymbol{\lambda}^T \dot{\mathbf{x}}) \, dt = (-\boldsymbol{\lambda}_f^T \dot{\mathbf{x}}_f) + (\boldsymbol{\lambda}_0^T \dot{\mathbf{x}}_0) + \int_{t_0}^{t_f} (\dot{\boldsymbol{\lambda}}^T \mathbf{x}) \, dt \tag{2.7}$$

Therefore:

$$J^* = \varphi + \boldsymbol{\mu}^T \boldsymbol{\psi} + (\boldsymbol{\lambda}_0^T \dot{\mathbf{x}}_0 - \boldsymbol{\lambda}_f^T \dot{\mathbf{x}}_f) + \int_{t_0}^{t_f} (\boldsymbol{\lambda}^T \boldsymbol{f} + \dot{\boldsymbol{\lambda}}^T \mathbf{x}) \, dt \tag{2.8}$$

One can now proceed to differentiate J^* and obtain:

$$\delta J^* = \left(\frac{\partial \varphi}{\partial t_0} + \boldsymbol{\mu}^T \frac{\partial \boldsymbol{\psi}}{\partial t_0} - H_0 \right) \delta t_0 + \tag{2.9a}$$

$$+ \left(\frac{\partial \varphi}{\partial t_f} + \boldsymbol{\mu}^T \frac{\partial \boldsymbol{\psi}}{\partial t_f} + H_f \right) \delta t_f + \tag{2.9b}$$

$$+ \left(\frac{\partial \varphi}{\partial \mathbf{x}_0} + \boldsymbol{\mu}^T \frac{\partial \boldsymbol{\psi}}{\partial \mathbf{x}_0} + \boldsymbol{\lambda}_0^T \right) \delta \mathbf{x}_0 + \tag{2.9c}$$

$$+ \left(\frac{\partial \varphi}{\partial \mathbf{x}_f} + \boldsymbol{\mu}^T \frac{\partial \boldsymbol{\psi}}{\partial \mathbf{x}_f} - \boldsymbol{\lambda}_f^T \right) \delta \mathbf{x}_f + \tag{2.9d}$$

$$+ \int_{t_0}^{t_f} \left[\left(\frac{\partial H}{\partial \mathbf{x}} + \dot{\boldsymbol{\lambda}}^T \right) \delta \mathbf{x} + \frac{\partial H}{\partial \mathbf{u}} \delta \mathbf{u} \right] dt \tag{2.9e}$$

where H is the system's Hamiltonian and is defined, in Mayer's formulation, as:

$$H \triangleq \boldsymbol{\lambda}^T \boldsymbol{f} \tag{2.10}$$

As mentioned, optimality requires $\delta J^* = 0$ for any admissible variation (δt_0, δt_f, $\delta \mathbf{x}_0$, $\delta \mathbf{x}_f$, $\delta \mathbf{x}$, and $\delta \mathbf{u}$). Therefore, an adequate set of Lagrange multipliers $\boldsymbol{\mu}$ and adjoint variables $\boldsymbol{\lambda}$ is to be defined.

2.2.3 Boundary Conditions for Optimality

In a Two Point Boundary Value Problem, boundary conditions for optimality are composed of a set of ODEs that define time (2 **transversality conditions**) and state ($2n$ **optimality conditions**) at the extremal points of the trajectory.

These boundary conditions arise by nullifying the coefficients of $\delta t_0, \delta t_f, \delta \mathbf{x}_0, \delta \mathbf{x}_f$ in equation (2.9):

$$\frac{\partial \varphi}{\partial t_0} + \boldsymbol{\mu}^T \frac{\partial \boldsymbol{\psi}}{\partial t_0} - H_0 = 0 \tag{2.11a}$$

$$\frac{\partial \varphi}{\partial t_f} + \boldsymbol{\mu}^T \frac{\partial \boldsymbol{\psi}}{\partial t_f} + H_f = 0 \tag{2.11b}$$

$$\frac{\partial \varphi}{\partial \mathbf{x}_0} + \boldsymbol{\mu}^T \frac{\partial \boldsymbol{\psi}}{\partial \mathbf{x}_0} + \boldsymbol{\lambda}_0^T = \mathbf{0} \tag{2.11c}$$

$$\frac{\partial \varphi}{\partial \mathbf{x}_f} + \boldsymbol{\mu}^T \frac{\partial \boldsymbol{\psi}}{\partial \mathbf{x}_f} - \boldsymbol{\lambda}_f^T = \mathbf{0} \tag{2.11d}$$

Boundary Conditions on Time:
From the two transversality equations (2.11a) and (2.11b):

- If initial or final time is not constrained and does not appear in φ, the corrisponding Hamiltonian is null and said time is dependent upon optimization;

- If time is assigned ($\boldsymbol{\psi}$ contains equations like $t_0 - t_a = 0$ or $t_f - t_b = 0$) the corresponding Hamiltonian is free and its value is dependent upon optimization.

Boundary Conditions on State Variables:
From the optimality conditions enunciated in equations (2.11c) and (2.11d):

- If the i-th state variable x_i is free at a certain point, i.e. it does not appear neither in $\boldsymbol{\psi}$ nor in any constraint, its associated adjoint variable λ_{x_i} is null at that point;

- If x_i is assigned, the corresponding adjoint variable is free at the same point.

2.2.4 Equations for adjoint and control variables

Imposing the last line of equation (2.9) equal to 0 yelds a set of ODEs that describes how adjoint variables and controls evolve over time, in particular:

- By nullifying the coefficients of $\delta\mathbf{x}$ the n **Euler-Lagrange equations for the adjoint variables** are obtained:

$$\frac{\partial\boldsymbol{\lambda}}{\partial t} = -\left(\frac{\partial H}{\partial\mathbf{x}}\right)^T \tag{2.12}$$

- By nullifying the coefficients of $\delta\mathbf{u}$ the m **algebraic equations for the control variables** arise:

$$\left(\frac{\partial H}{\partial\mathbf{u}}\right)^T = 0 \tag{2.13}$$

In general one or more control variables may be subject to external constraints, so that $\mathbf{u} \in \boldsymbol{U}$, where $\boldsymbol{U}$ represents the admissibility domain. A specific control may be dependent on state variables and on time; in this work only explicit and constant constraints are dealt with, like limiting a control to a maximum and minimum value: $U_{min} \leq u \leq U_{max}$. If explicit admissibility constraints are present, the optimal control $\mathbf{u}^* \in \boldsymbol{U}$ for the optimal trajectory is the one that maximizes the Hamiltonian in each point of the trajectory. This concept is known as Pontryagin's Maximum Principle (PMP).

In practice, two cases arise:

- The optimal control value $\mathbf{u}^*$ provided by equation (2.13) belongs to the admissibility domain: the control constraint is not active in that point (the control is locally un-constrained);

- The optimal control value $\mathbf{u}^*$ provided by equation (2.13) doesn't belong to the admissibility domain: the optimal control is set to the edge of the admissibility domain (the control is locally constrained).

When the Hamiltonian is linear (affine) with respect to a specific control variable, equation (2.13) cannot be satisfied. In such cases, the control variable does not appear explicitly in the equation, rendering the corresponding control undetermined.

In the case of a Hamiltonian that is affine with a control variable u_i:

$$\frac{\partial H}{\partial u_i} = k_{u_i} \tag{2.14}$$

with k_{u_i} being constant, it is evident that Equation (2.13) cannot hold true, except for when $k_{u_i} = 0$. To resolve this, the Pontryagin Maximum Principle (PMP) is utilized to determine the value of the control variable [8]. If $k_{u_i} \neq 0$, maximizing the Hamiltonian involves setting the control variable to either its maximum admissible value, $u_i = U_{i,max}$, when $k_{u_i} > 0$, or its minimum admissible value, $u_i = U_{i,min}$, when $k_{u_i} < 0$. This condition is commonly referred to as "bang-bang" control, and it will be the implemented control strategy in the optimal control problem considered in this work.

If $k_{u_i} = 0$ during a finite time interval, a strategy involving singular arcs must be adopted.

The problem presented so far is a Two-Point Boundary Value Problem: with the imposed boundary conditions $\boldsymbol{\psi} = \mathbf{0}$ (q equations), one has $2n + q + 2$ equations, respectively from optimality ((2.11c) and (2.11d)), control (2.13) and transversality (eq. (2.11a) and (2.11b)), which implicitly determine the initial values for $2n$ differential equations (n states $\mathbf{x}$ and n costates $\boldsymbol{\lambda}$), q adjoint constants ($\boldsymbol{\mu}$) and 2 times (t_0 and t_f).

2.3 Multi-Point Boundary Value Problem

If a mission imposes any constraints in internal points along the trajectory, such as specified functions of state variables or variables discontinuities, the resulting optimization problem is a Multi-Point BVP (MPBVP). The trajectory is divided into n_p subintervals, called phases or arcs, so that the integration can be split into n_p intervals at the relevant $(n_p - 1)$ intermediate points. The j-th interval spans from $t_{(j-1)+}$ to $t_{(j)-}$ and the variable values at the extremities of said interval are $\mathbf{x}_{(j-1)+}$ and $\mathbf{x}_{(j)-}$ respectively, where $j = 1, ..., f$.

Due to the added complexity of the problem, this work does not implement the MPBVP formulation and instead focuses on the resolution of TPBVPs. For the sake of completeness, some basic information regarding MPBVPs is provided below; for further details please refer to [3].

As anticipated, in a MPBVP, boundary conditions can be imposed at the internal boundaries in addition to the external boundaries seen in equation (2.2). BCs are again generally Non Linear and may be function of both the state variables and the independent time variable:

$$\boldsymbol{\psi}\left(\mathbf{x}_{(j-1)+}, \mathbf{x}_{(j)-}, t_{(j-1)+}, t_{(j)-}\right) = \mathbf{0}, \quad j = 1, ..., n_p \qquad (2.15)$$

The performance index for the MPBVP is defined as:

$$J = \boldsymbol{\varphi}(\mathbf{x}_0, \mathbf{x}_{1\pm}, ..., \mathbf{x}_f, t_0, t_{1\pm}, ..., t_f) + \sum_{j=1}^{n_p} \int_{t_{(j-1)+}}^{t_{(j)-}} [\boldsymbol{\Phi}(\mathbf{x}(t), \mathbf{u}(t), t)] \, dt \qquad (2.16)$$

Where $\boldsymbol{\varphi}$ is now dependent on the values that variables and times have at every boundary. The summation of all the integrals of $\boldsymbol{\Phi}$ still depends on the values that the state variables, controls and time assume during the trajectory and now accounts for how the solution evolves arc-by-arc.

The augmented merit index J^* can now be obtained; in Meyer's formulation, it has the form:

$$J^* = \boldsymbol{\varphi} + \boldsymbol{\mu}^T \boldsymbol{\psi} + \sum_{j=1}^{n_p} \int_{t_{(j-1)+}}^{t_{(j)-}} [\boldsymbol{\lambda}^T(\boldsymbol{f} - \dot{\mathbf{x}})] \, dt \qquad (2.17)$$

which can be integrated by part to obtain:

$$J^* = \boldsymbol{\varphi} + \boldsymbol{\mu}^T \boldsymbol{\psi} + \sum_{j=1}^{n_p} \left(\boldsymbol{\lambda}_{(j-1)+}^T \dot{\mathbf{x}}_{(j-1)+} - \boldsymbol{\lambda}_{(j)-}^T \dot{\mathbf{x}}_{(j)-}\right) + \sum_{j=1}^{n_p} \int_{t_{(j-1)+}}^{t_{(j)-}} (\boldsymbol{\lambda}^T \boldsymbol{f} + \dot{\boldsymbol{\lambda}}^T \mathbf{x}) \, dt$$

$$\qquad (2.18)$$

11

The first order differentiation of J^*, δJ^*, is now expressed per each arc as:

$$\delta J^* = \left(\frac{\partial \boldsymbol{\varphi}}{\partial t_{(j-1)+}} + \boldsymbol{\mu}^T \frac{\partial \boldsymbol{\psi}}{\partial t_{(j-1)+}} - H_{(j-1)+} \right) \delta t_{(j-1)+} + \tag{2.19a}$$

$$+ \left(\frac{\partial \boldsymbol{\varphi}}{\partial t_{(j)-}} + \boldsymbol{\mu}^T \frac{\partial \boldsymbol{\psi}}{\partial t_{(j)-}} + H_{(j)-} \right) \delta t_{(j)-} + \tag{2.19b}$$

$$+ \left(\frac{\partial \boldsymbol{\varphi}}{\partial \mathbf{x}_{(j-1)+}} + \boldsymbol{\mu}^T \frac{\partial \boldsymbol{\psi}}{\partial \mathbf{x}_{(j-1)+}} + \boldsymbol{\lambda}_{(j-1)+}^T \right) \delta \mathbf{x}_{(j-1)+} + \tag{2.19c}$$

$$+ \left(\frac{\partial \boldsymbol{\varphi}}{\partial \mathbf{x}_{(j)-}} + \boldsymbol{\mu}^T \frac{\partial \boldsymbol{\psi}}{\partial \mathbf{x}_{(j)-}} - \boldsymbol{\lambda}_f^T \right) \delta \mathbf{x}_{(j)-} + \tag{2.19d}$$

$$+ \sum_{j=1}^{n_p} \int_{t_{(j-1)+}}^{t_{(j)-}} \left[\left(\frac{\partial H}{\partial \mathbf{x}} + \dot{\boldsymbol{\lambda}}^T \right) \delta \mathbf{x} + \frac{\partial H}{\partial \mathbf{u}} \delta \mathbf{u} \right] dt, \quad j = 1, ..., n_p \tag{2.19e}$$

Boundary Conditions for Optimality
Optimality and Transversality conditions are more conveniently expressed at the generic point j:

$$\frac{\partial \boldsymbol{\varphi}}{\partial t_{j+}} + \boldsymbol{\mu}^T \frac{\partial \boldsymbol{\psi}}{\partial t_{j+}} - H_{j+} = 0 \quad j = 1, ..., n_p - 1 \tag{2.20a}$$

$$\frac{\partial \boldsymbol{\varphi}}{\partial t_{j-}} + \boldsymbol{\mu}^T \frac{\partial \boldsymbol{\psi}}{\partial t_{j-}} + H_{j-} = 0 \quad j = 1, ..., n_p \tag{2.20b}$$

$$\frac{\partial \boldsymbol{\varphi}}{\partial \mathbf{x}_{j+}} + \boldsymbol{\mu}^T \frac{\partial \boldsymbol{\psi}}{\partial \mathbf{x}_{j+}} + \boldsymbol{\lambda}_{j+}^T = \mathbf{0} \quad j = 1, ..., n_p - 1 \tag{2.20c}$$

$$\frac{\partial \boldsymbol{\varphi}}{\partial \mathbf{x}_{j-}} + \boldsymbol{\mu}^T \frac{\partial \boldsymbol{\psi}}{\partial \mathbf{x}_{j-}} - \boldsymbol{\lambda}_{j-}^T = \mathbf{0} \quad j = 1, ..., n_p \tag{2.20d}$$

Equations for adjoint and control variables
Considerations on Euler-Lagrange and control equations remain identically true in the Multi-Point formulation of the OCP.

Significant difficulties in the MPBVP convergence arise when the relevant times are unknown and the lenghts of the integration intervals are free. In order to fix the extremes of the integration intervals of each arc, a transformation of the independent variable (time, t) is operated, so that in the j-th arc, t is replaced by:

$$\epsilon = j - 1 + \frac{t - t_{j-1}}{t_j - t_{j-1}} = j - 1 + \frac{t - t_{j-1}}{\tau_j} \tag{2.21}$$

Where $\tau_j \triangleq t_j - t_{j-1}$ is unknown and subject to optimization. In the j-th arc, ϵ varies between j-1 and j, hence assumes consecutive integer values at the boundaries of the interval.

The state ODEs during the j-th arc become:

$$\dot{\mathbf{x}}(t) = \frac{d\mathbf{x}(t)}{d\epsilon} = \tau_j \frac{d\mathbf{x}(t)}{dt} \tag{2.22}$$

2.4 Numerical Methods for Indirect Optimization

The analytical solution for the BVPs above illustrated is usually impossible to obtain, especially when the system dynamics is non-linear; therefore, proper numerical methods have to be employed. The most well-known methods to solve the BVP numerically are the shooting techniques; collocation methods are also exploited to solve generic BVPs. Besides these general-purpose methods, a sequential gradient restoration algorithm can be implemented to solve BVPs that originate from OCPs.

- Shooting methods transform the Boundary Value Problem into an Initial Value Problem (IVP), which can be solved via well-established algorithms and led to convergence by Newton-like or gradient methods. They are easy to understand and very efficient, but their efficacy is strongly linked to the behaviour of the IVP.

- Collocation methods search for an approximate solution over the entire interval of interest, hence no initial value problem is explicitly integrated. This allows for a more global approach to the BVP solution, avoiding convergence issues caused by IVP instability. These methods' computational efficiency is lower than the shooting techniques' since they rely on low order quadrature schemes [5].

- Sequential Gradient Restoration relies on the solution of many auxiliary linear TPBVPs, the solution of the original problem is found iteratively, after performing a sequence of gradient restoration steps.

Due to their straight-forward implementation and high efficiency, shooting techniques are the implemented numerical method to solve the BVPs in this work.

2.4.1 Single Shooting Method

The "shooting" procedure consists in finding the initial values for the state, costate and unknown parameters, which guarantee the satisfaction of all boundary conditions. Dependent variables at the boundaries are obtained via numerical integration

of the ODE system, once initial conditions are provided. Starting from an initial guess, initial conditions are adjusted exploiting Newton-like or gradient based methods through a process of differential correction. In other words, the BVP that describes a trajectory optimization problem is transformed into an Initial Value Problem (IVP), which is iteratively solved via numerical integration in order to compute corrections (through a differential corrector) for undesired terminal deviation, updating the initial conditions at each r-th iteration. It is important noting that not all initial values may be allowed to vary, and some final conditions may be free to aquire any feasible value; therefore, the divergence between the desired final state and the actual one should imply a correction only to the initial guesses that are allowed to vary.

Let $\mathbf{y} \in \mathbb{R}^{2n+p}$ be the vector that collects state $\mathbf{x}(t)$ and adjoint $\boldsymbol{\lambda}(t)$ variables and unknown parameters $\mathbf{c} \in \mathbb{R}^p$:

$$\mathbf{y}(t) = (\mathbf{x}(t), \boldsymbol{\lambda}(t), \mathbf{c})^T \tag{2.23}$$

and $\mathbf{y}_0$ be the initial conditions vector.

The result of a shooting method is the *Shooting Function S*, which associates to any initial conditions vector a residual on the boundary conditions:

$$S : \mathbb{R}^{(2n+p)} \to \mathbb{R}^{(2n+p)}$$
$$\mathbf{y}_0 \rightarrowtail \boldsymbol{\psi}(\mathbf{Y}_+(\mathbf{y}_0), \mathbf{T}_+(\mathbf{y}_0), \mathbf{Y}_-(\mathbf{y}_0), \mathbf{T}_-(\mathbf{y}_0)) \tag{2.24}$$

where $\mathbf{Y}_+$ and $\mathbf{Y}_-$ are two vectors that collect the values that $\mathbf{y}$ assumes at either side of the boundaries:

$$\mathbf{Y}_+ = \left\{ \mathbf{y}_{(j-1)+}, \forall j = 1, ..., n_p \right\} \quad \mathbf{Y}_- = \left\{ \mathbf{y}_{j-}, \forall j = 1, ..., n_p \right\} \tag{2.25}$$

The roots of the shooting function provide the BVP solution.

The appeal of this approach is justified by its simplicity and strenghtened by the state-of-the-art of numerical analysis for IVPs. However, there is no guarantee of convergence for this method under general assumptions: single shooting is usually successfull if the ODE system is not severely unstable or very stiff and if a good initial estimate of $\mathbf{y}_0$ can be made. A good $\mathbf{y}_0$ guess is required because shooting with a wrong initial estimate may lead to an IVP whose solution doesn't exist over the whole integration domain, which would prevent the convergence of the iterative process. The main difficulty with the indirect approach to trajectory optimization is linked to the adjoint variables (or costates). Initial values for the costates are unknown and the non-linearity of the problem implies that the course of the solution is very sensitive to some or all of these initial adjoint variables. Moreover, the problem's costates lack of the physical significance of the state variables, so estimating an initial guess can be quite challenging. IVP stability is another requirement to guarantee stability of the algorithm.

2.4.2 Multiple Shooting

The multiple shooting technique is a variant of the single shooting that aims to enlarge its applicability field and reduce its drawbacks. A multiple shooting approach splits the integration interval, hence the trajectory, into subintervals at specified points. Analogously to single shooting, the values of the dependent variables at the beginning of each sub-arc are treated as problem unknowns. Proper boundary conditions are introduced to guarantee trajectory continuity at the interfaces of each sub-domain and separate integrations over each sub-interval are performed, thus reducing the influence of the initial guess on the error. Convergence is usually easier, at the expense of a larger number of unknowns, hence increased computational times and a more difficult formulation of the problem. For these reasons, the simple shooting technique is preferred in this work.

2.5 Differential Correction

The differential correction procedure aims at nullifying the difference between the desired final state $\mathbf{y}_f^*$ and the one obtained via IVP resolution $\mathbf{y}_f$. Let $\delta\mathbf{y}_f$ be the discrepancy between the desired and the actual final states:

$$\delta\mathbf{y}_f = \mathbf{y}(\mathbf{y}_0, t_f) - \mathbf{y}^*(\mathbf{y}_0^*, t_f) \tag{2.26}$$

A specific correction in the initial state, say $\delta\mathbf{y}_0$, should produce the needed initial state $\mathbf{y}_0^*$:

$$\mathbf{y}_0^* = \mathbf{y}_0 + \delta\mathbf{y}_0 \tag{2.27}$$

A first order Taylor expansion of the constraint vector $\boldsymbol{\psi}$ is performed to evaluate how to update the initial state:

$$\boldsymbol{\psi}(\mathbf{y}) = \boldsymbol{\psi}(\mathbf{y}_0) + \frac{\partial\boldsymbol{\psi}(\mathbf{y_0})}{\partial\mathbf{y}}(\mathbf{y} - \mathbf{y}_0) \tag{2.28}$$

The derivatives of the constraints with respect to the state vector quantities form a Jacobian matrix $\boldsymbol{G}(\boldsymbol{\psi}(\mathbf{y}_0), \mathbf{y}) \in \mathbb{R}^{q \times 2n}$ that can be referred to as *Error Gradient Matrix*:

$$\boldsymbol{G}(\boldsymbol{\psi}(\mathbf{y}_0), \mathbf{y}) = \frac{\partial\boldsymbol{\psi}(\mathbf{y_0})}{\partial\mathbf{y}} = \begin{pmatrix} \frac{\partial\psi_1}{\partial y_1} & \frac{\partial\psi_1}{\partial y_2} & \cdots & \frac{\partial\psi_1}{\partial y_{2n}} \\ \frac{\partial\psi_2}{\partial y_1} & \frac{\partial\psi_2}{\partial y_2} & \cdots & \frac{\partial\psi_2}{\partial y_{2n}} \\ \vdots & \vdots & \ddots & \vdots \\ \frac{\partial\psi_q}{\partial y_1} & \frac{\partial\psi_q}{\partial y_2} & \cdots & \frac{\partial\psi_q}{\partial y_{2n}} \end{pmatrix} \tag{2.29}$$

The error gradient matrix linearly maps the variation of the errors on the boundary conditions to the variations of the initial state. It can be obtained analytically, but this procedure is usually rather heavy both in terms of analytical

15

effort to obtain the necessary equations, and time to program and debug the code, and also implies larger computational costs [9]. Thus the analytical approach should be employed only when other numerical techniques fail to provide convergence. In this work a numerical method is adopted.

2.5.1 Newton's Method

The values of the error gradient matrix $\boldsymbol{G}$, are obtained by varying the unknowns by a small amount and solving the IVP problem with the new perturbed initial conditions vector. The correction of the tentative values is thus obtained under a linear approximation.

Let r represent the current step of the iterative shooting procedure: $(\mathbf{y}_0)_r$ is perturbed by a small delta in its i-th component in order to obtain the error gradient matrix's i-th column. According to a forward-finite-difference scheme: Let $[(\mathbf{y}_0)_r]_p$ be the perturbed initial state:

$$[(\mathbf{y}_0)_r]_p = (\mathbf{y}_0)_r + e_i \cdot \Delta \tag{2.30}$$

where e_i is a 2n-component-unit-vector, with all elements equal to zero except for the i-th element. Then the i-th column of the error gradient matrix is:

$$\boldsymbol{G}_r[:,i] = \frac{[(\boldsymbol{\psi}(\boldsymbol{y}_0))_r]_p - (\boldsymbol{\psi}(\boldsymbol{y}_0))_r}{\Delta} \tag{2.31}$$

The r+1 initial guess is then defined as:

$$(\mathbf{y}_0)_{r+1} = (\mathbf{y}_0)_r - \boldsymbol{G}_r^{-1}(\boldsymbol{\psi}(\boldsymbol{y}_0))_r \tag{2.32}$$

Linearization may introduce errors that can prevent convergence and induce instability; for this reason two relaxation parameters are introduced, K_1 and K_2. Both reduce the parameter correction: K_1 is utilized performing a check on error variation and reducing, usually by half, parameter correction if $\max(\boldsymbol{\psi}_{r+1}) > K_1\max(\boldsymbol{\psi}_r)$. This operation is known as bisection; the bisection parameter K_1 is usually equal to 2. K_2 is introduced in the correction scheme:

$$(\mathbf{y}_0)_{r+1} = (\mathbf{y}_0)_r - K_2\boldsymbol{G}_r^{-1}(\boldsymbol{\psi}(\boldsymbol{y}_0))_r \tag{2.33}$$

K_2 is usually set in the range $0.01 \leq K_2 \leq 1$ but its efficacy is strongly dependent on the closeness of the initial state to the actual solution and on the overall problem dimensions. The closer to the solution, the greater K_2 can be.

2.6   The Rocket Sled Problem

In this section, an illustrative example is presented in order to clarify how an optimal control problem can be solved via indirect optimization and a single shooting procedure. The one-dimensional problem under investigation consists of a mass point that has to cover a fixed distance in a fixed time, arriving and departing with zero velocity. The maximum value of acceleration or deceleration provided by the control is limited and the goal is to minimize the control consumption, i.e. maximize the final mass.

The mathematical formulation of the OCP is:

$$OCP = \begin{cases} \max \quad J = m_f \\[1em] \begin{cases} \dot{\mathbf{r}}(t) = \mathbf{v}, & t \in [0, t_f] \\[0.5em] \dot{\mathbf{v}}(t) = \mathbf{T}/m, & t \in [0, t_f] \\[0.5em] \dot{m}(t) = -T/c, & t \in [0, t_f] \end{cases} \\[2em] s.t. \\[1em] |T| \leq T_{\max} \\[0.5em] r_i = 0; \quad r_f = 0.1 \\[0.5em] v_i = 0; \quad v_f = 0 \\[0.5em] m_i = 1; \quad m_f = \text{free} \end{cases} \tag{2.34}$$

The state and costate vectors for this OCP are defined as:

$$\mathbf{x}(t) = (\mathbf{r}, \mathbf{v}, m)^T \quad \boldsymbol{\lambda}(t) = (\lambda_r, \lambda_v, \lambda_m)^T \tag{2.35}$$

and the control variables vector is:

$$\mathbf{u}(t) = (T) \tag{2.36}$$

The Hamiltonian can now be stated:

$$H = \boldsymbol{\lambda}^T f = \lambda_r v + \lambda_v \frac{T}{m} - \lambda_m \frac{T}{c} = \lambda_r(v) + \frac{T}{m}\left[\lambda_v - \lambda_m \frac{m}{c}\right] \tag{2.37}$$

Since the Hamiltonian is linear with the control variable T, a bang-bang control rises and a switching function SF can be defined:

$$SF = \lambda_v - \lambda_m(m/c) \tag{2.38}$$

Usually, in order to maximize the Hamiltonian, the control variable would be set to its upper boundary, T_{max} when the switching function is positive and to its lower boundary, zero, when the SF is negative. In this example this bang-bang control strategy would prevent the point-mass from decelerating since there is no control on the direction of thrust, therefore, the control strategy is slightly modified as follows:

$$T = \begin{cases} T_{max}, & if \quad SF > 1 \\ 0, & if \quad -1 < SF < 1 \\ -T_{max}, & if \quad SF < -1 \end{cases} \tag{2.39}$$

The Euler-Lagrange equations for the adjoint variables are:

$$\frac{d\lambda_r}{dt} = -\frac{\partial H}{\partial r} = 0 \tag{2.40a}$$

$$\frac{d\lambda_v}{dt} = -\frac{\partial H}{\partial v} = -\lambda_r \tag{2.40b}$$

$$\frac{d\lambda_m}{dt} = -\frac{\partial H}{\partial m} = \lambda_v \frac{T}{m^2} \tag{2.40c}$$

The Two Point BVP is now completely defined and can be solved via numerical integration. Within the Scipy "solve ivp" environment in Python, an explicit Runge-Kutta method of order 8 was exploited to integrate this problem's ODEs.
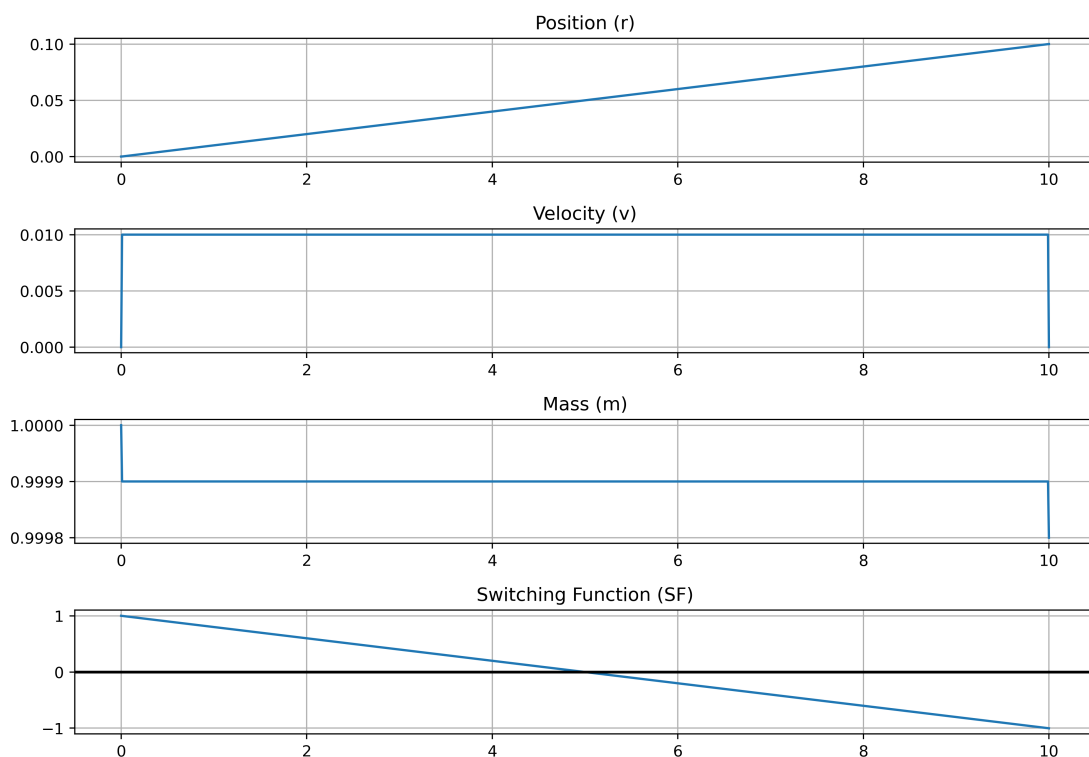
Figure 2.1: Rocket Sled Example: state variables, mass and switching function during the maneuver. $T_{\max} = 1$, $c = 100$

The solution obtained exhibits an initial acceleration determined by the switching function being grater than 1 for a brief moment, followed by a lenghty coasting phase in which $-1 < SF < 1$. A final deceleration is provided ($SF < -1$) to reach the end point with a null trajectory.

2.6.1 Two Dimensional Example

The same problem can now be stated adding a degree of freedom: the point mass is now free to move on the x-y plane. Initial and final y positions are the same in

order to replicate the previous example. The following OCP is defined:

$$
\text{OCP} =
\begin{cases}
\max \quad J = m_f \\[2mm]
\begin{cases}
\dot{\mathbf{x}}(t) = \mathbf{v_x}, & t \in [0, t_f] \\[2mm]
\dot{\mathbf{y}}(t) = \mathbf{v_y}, & t \in [0, t_f] \\[2mm]
\dot{\mathbf{v}}_{\mathbf{x}}(t) = \frac{\mathbf{T}}{m}\cos(\alpha), & t \in [0, t_f] \\[2mm]
\dot{\mathbf{v}}_{\mathbf{y}}(t) = \frac{\mathbf{T}}{m}\sin(\alpha), & t \in [0, t_f] \\[2mm]
\dot{m}(t) = -\frac{T}{c}, & t \in [0, t_f]
\end{cases} \\[2mm]
\text{s.t.} \\[2mm]
\quad T \le T_{\max} \\[2mm]
\quad x_i = 0; \quad x_f = 0.1 \\[2mm]
\quad y_i = 0; \quad y_f = 0 \\[2mm]
\quad v_{xi} = 0; \quad v_{xf} = 0 \\[2mm]
\quad v_{yi} = 0; \quad v_{yf} = 0 \\[2mm]
\quad m_i = 1; \quad m_f = \text{free}
\end{cases}
\tag{2.41}
$$

Where α is the thrust angle and represents the second control variable: the control variable vector is now $\mathbf{u}(t) = (T, \alpha)$. The Hamiltonian for this OCP is:

$$
H = \boldsymbol{\lambda}^T f = \lambda_x v_x + \lambda_y v_y + \lambda_{vx}\frac{T}{m}\cos(\alpha) + \lambda_{vy}\frac{T}{m}\sin(\alpha) - \lambda_m \frac{T}{c}
\tag{2.42}
$$

Optimal Control Equations for the control variables are:

$$
\frac{\partial H}{\partial T} = 0
\tag{2.43a}
$$

$$
\frac{\partial H}{\partial \alpha} = 0
\tag{2.43b}
$$

Equation (2.43a) yelds the same result as the 1D optimal control equation: the Hamiltonian is linear with the Thrust and therefore a bang-bang control is adopted; equation (2.43b) provides the optimal thrust direction as a function of the costates:

$$
\alpha = arctan\left(\frac{\lambda_{vy}}{\lambda_{vx}}\right)
\tag{2.44}
$$

It follows that now the point-mass can accelerate or decelerate deliberately so a normal bang-bang control can be utilized:

$$T = \begin{cases} T_{\max}, & \text{if } SF > 0 \\ 0, & \text{if } SF < 0 \end{cases} \tag{2.45}$$

where the switching funcion is defined as:

$$SF = \lambda_{vx}\cos(\alpha) + \lambda_{vy}\sin(\alpha) - \lambda_m(m/c) \tag{2.46}$$

The Euler-Lagrange equations for the adjoint variables are obtained the same way as previously. The obtained TPBVP was solved with the same numerical method and the following results were obtained:
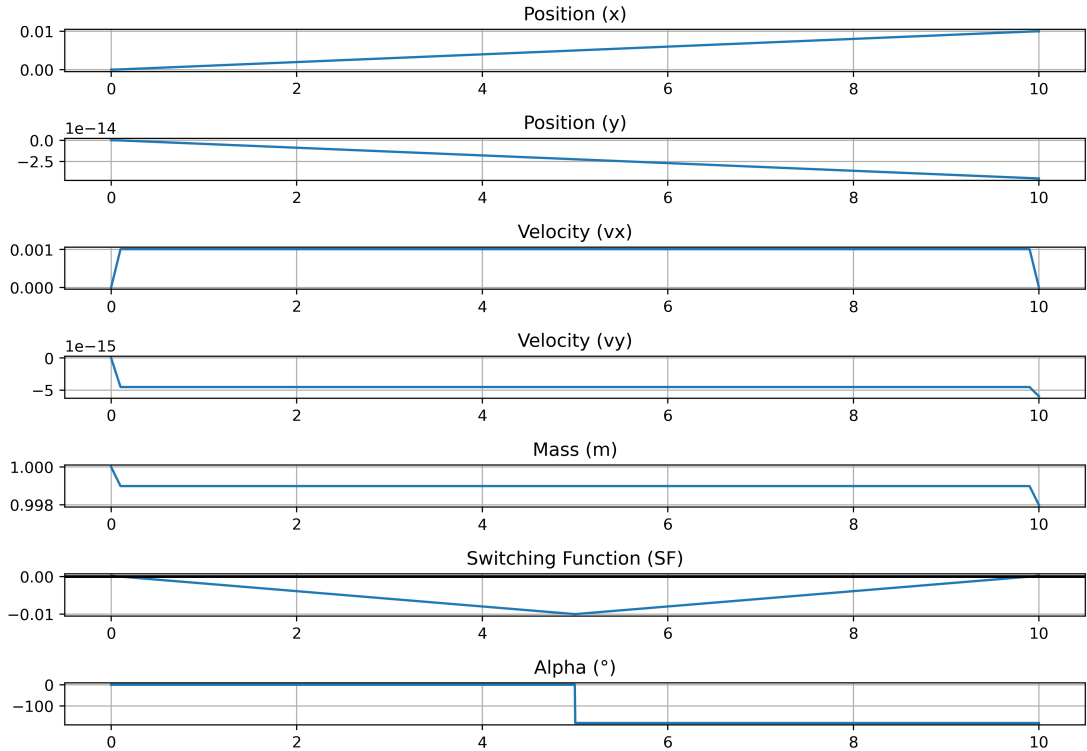
Figure 2.2: 2D Example: state variables, mass, switching function and thrust angle during the maneuver. $T_{\max} = 1$, $c = 100$

It is possible to observe that the solution to the 2D trajectory optimization problem is nearly identical to the one-dimensional case, despite the control laws

employed being different. In the two-dimensional case, when the "rocket sled" must decelerate, thrust is provided along the velocity vector with opposite direction, as it is denoted by $\alpha = -180°$ in the graph above. The position and velocity values along the y-axis are negligible since they approach machine precision. By incrementally introducing additional complexities into the trajectory optimization problem through a systematic, step-by-step approach, it is possible to validate the novel tool by reproducing the preceding scenario. This methodology was employed to ultimately develop a three-dimensional trajectory optimization tool incorporating two-body dynamics.

Chapter 3

Dynamic Model

This chapter introduces the dynamic model implemented in the optimization framework (in section 3.3) as well as the main reference systems used during the analysis and main coordinate transformations required (in section 3.1). Furthermore the perturbations considered in the high-fidelity orbit propagator employed in the collision risk evaluation tool are presented in section 3.4.

3.1 Reference systems

A generic reference system is uniquely defined by its origin, a fundamental plane and an orthonormal right-handed triad forming the reference frame (RF). Reference systems can be inertial, in which Newton's first law holds true, or non-inertial; the choice of using one or the other is dictated by which is more suitable to a specific analysis. The primary distinction between inertial and non-inertial reference systems can be attributed to the presence or absence of apparent accelerations resulting from relative observations. For instance, in non-inertial reference systems such as rotating frames, additional pseudo-accelerations such as the Coriolis effect manifest. The description of the motion of objects such as satellites or celestial bodies in relation to the Earth is straightforward within an inertial reference system. This allows the use of various coordinate systems, such as cartesian or polar coordinates, for the accurate representation of the objects' positions.

3.1.1 EME2000 RF

In the present work the geocentric-equatorial reference system coincides with the Earth Mean Equator and equinox of epoch J2000 (EME2000). The JPL DE440 ephemerides utilised in this analysis encompass nutations and librations with respect to the Inertial Celestial Reference Frame (ICRF), thereby rendering the

EME2000 RF (also known as J2000) a quasi-inertial reference system. However, since the rotational offset between the ICRF and the J2000 is minimal, the latter will be considered inertial in this work. The J2000 RF has its origin at the Earth's center, its reference plane is the equatorial plane and its unit vectors $\hat{\boldsymbol{I}}, \hat{\boldsymbol{J}}, \hat{\boldsymbol{K}}$ have $\hat{\boldsymbol{I}}$ pointing towards the vernal equinox, $\hat{\boldsymbol{K}}$ normal to the reference plane and $\hat{\boldsymbol{J}}$ completing the triad.

3.1.2 Perifocal RF

The perifocal RF has its origin at the center of the gravitational body and its reference plane contains the satellite's motion. Its unit vectors are $\hat{\boldsymbol{p_{sc}}}, \hat{\boldsymbol{q_{sc}}}, \hat{\boldsymbol{w_{sc}}}$, where the $\hat{\boldsymbol{p_{sc}}}$ unit vector coincides with the eccentricity vector direction $\hat{\boldsymbol{e}}$, $\hat{\boldsymbol{w_{sc}}}$ is normal to the orbital plane and pointing towards the direction of the specific angular momentum vector $\hat{\boldsymbol{h}}$, and $\hat{\boldsymbol{q_{sc}}}$ completes the triad. The shape and orientation of a conic in space can be described by a set of parameters such as the Keplerian ones: $a, e, i, \Omega, \omega, \nu$ uniquely define the orbit's geometry and orientation while also identifying the spacecraft's position. A subset of these parameters is sufficient for the perifocal representation as the conic equation shows:

$$r = \frac{a\left(1 - e^2\right)}{1 + e\cos(\nu)} \tag{3.1}$$

The true anomaly ν identifies the angular position of the spacecraft, while the semi-major axis a and the eccentricity e fully define a closed orbit.

To orient the perifocal RF in the three dimensional space (with respect to J2000) the remaining three Keplerian parameters are needed. In particular, the inclination i identifies the angle between the equatorial and perifocal planes, the right ascension of ascending node (RAAN) Ω identifies the engle between $\hat{\boldsymbol{I}}$ and the intersection between the two reference planes where the spacecraft passes from the southern to the northern hemisphere (line of nodes $\hat{\boldsymbol{n}}$), and the argument of the periapsis ω identifies the angle between the line of nodes and the periapsis, for non-circular orbits.

3.1.3 ZEN RF

The Zenith-East-North reference frame has its origin in the spacecraft's center of mass, which makes it a non-inertial frame. Its unit vectors $\hat{\boldsymbol{u}}, \hat{\boldsymbol{v}}, \hat{\boldsymbol{w}}$ conveniently describe the SC's velocity components in radial, tangential and normal directions, respectively. The radial direction is determined by extending the position vector of the spacecraft from the center of the Earth. The tangential and normal directions correspond to the orientations of a parallel and a meridian on a celestial sphere.

3.1.4 ITFR93 RF

The International Terrestrial Reference Frame (ITRF) 93 is a geocentric reference frame established in 1993. It serves as a standard coordinate system for global positioning and geodetic and atmospheric measurements. ITRF93 is geocentric, has the equatorial plane as reference plane and unit vectors $\hat{\boldsymbol{X}}, \hat{\boldsymbol{Y}}, \hat{\boldsymbol{Z}}$ with $\hat{\boldsymbol{X}}$ laying on the reference plane and positive through the intersection with the prime meridian, $\hat{\boldsymbol{Y}}$ positive through 0° N, 90° E, and $\hat{\boldsymbol{Z}}$ axis parallel to the mean Earth rotation axis and positive toward the North Pole.

3.2 Time-invariant coordinate transformation

For specific computations or better understanding of the information provided by a set of coordinates it is sometimes necessary to switch between reference frames. For this purpose, simple elementary rotational matrices are implemented. These matrices are composed of a series of Direction Cosine Matrices (DCMs). For a generic positive rotation of α the DCMs are defined in the following form:

$$\boldsymbol{R}_1 = \begin{bmatrix} 1 & 0 & 0 \\ 0 & c(\alpha) & s(\alpha) \\ 0 & -s(\alpha) & c(\alpha) \end{bmatrix}, \boldsymbol{R}_2 = \begin{bmatrix} c(\alpha) & 0 & s(\alpha) \\ 0 & 1 & 0 \\ -s(\alpha) & 0 & c(\alpha) \end{bmatrix}, \boldsymbol{R}_3 = \begin{bmatrix} c(\alpha) & s(\alpha) & 0 \\ -s(\alpha) & c(\alpha) & 0 \\ 0 & 0 & 1 \end{bmatrix}$$

where s and c stand for sin and cos respectively.
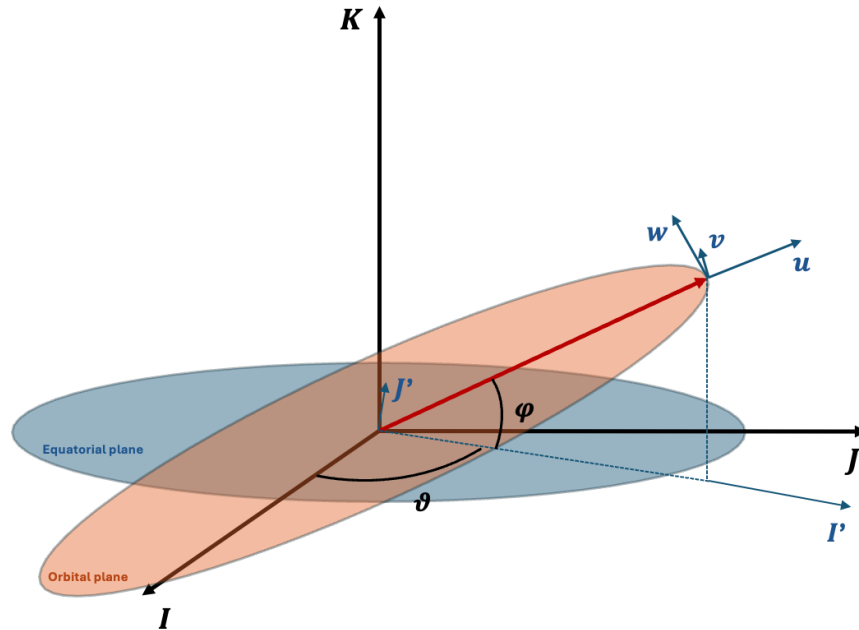

Figure 3.1: from J2000 RF to ZEN RF

As an example, the transformation between J2000 coordinates to ZEN coordinates, depicted above, is achieved with the following steps:

- A first rotation of θ about the $\hat{\boldsymbol{K}}$ axis is performed:

$$\boldsymbol{r}_{\hat{\boldsymbol{I}}',\hat{\boldsymbol{J}}',\hat{\boldsymbol{K}}} = \boldsymbol{R}_3(\theta)\boldsymbol{r}_{\hat{\boldsymbol{I}},\hat{\boldsymbol{J}},\hat{\boldsymbol{K}}} \tag{3.2}$$

- Now a second rotation of ϕ about the $\hat{\boldsymbol{J}}'$ is needed:

$$\boldsymbol{r}_{\hat{\boldsymbol{u}},\hat{\boldsymbol{v}},\hat{\boldsymbol{w}}} = \boldsymbol{R}_2(\phi)\boldsymbol{r}_{\hat{\boldsymbol{I}}',\hat{\boldsymbol{J}}',\hat{\boldsymbol{K}}} \tag{3.3}$$

While described as being carried out with individual steps, the coordinate transformation can be performed in a single operation by defining the complete rotational matrix:

$$\boldsymbol{R}_{32}(\theta, \phi) = \boldsymbol{R}_2(\phi) \cdot \boldsymbol{R}_3(\theta) \tag{3.4}$$

so that the coordinate transformation can be written as:

$$\boldsymbol{r}_{\hat{\boldsymbol{u}},\hat{\boldsymbol{v}},\hat{\boldsymbol{w}}} = \boldsymbol{R}_{32}(\theta, \phi) \cdot \boldsymbol{r}_{\hat{\boldsymbol{I}},\hat{\boldsymbol{J}},\hat{\boldsymbol{K}}} \tag{3.5}$$

3.3 Two Body Problem

The two-body problem in astrodynamics involves the gravitational interaction between two celestial bodies, typically a central body and an orbiting body. In this scenario, the influence of other celestial bodies is assumed to be negligible. The motion of the orbiting body is governed by conservation principles such as energy and angular momentum, along with Kepler's laws of planetary motion describing its orbit. This simplified model well describes the motion of a spacecraft orbiting the Earth in LEO because other significant gravitational masses, such as the Moon and Sun, are much farther away than the Earth and their effect on the spacecraft's orbit is negligible in preliminary analysis [10].

The state of a SC is described by the following set of ODEs in an inertial RS centered in the primary celestial body, such as J2000.

$$\frac{d\boldsymbol{r}}{dt} = \boldsymbol{V} \tag{3.6a}$$

$$\frac{d\boldsymbol{V}}{dt} = \boldsymbol{g} + \frac{\boldsymbol{T}}{m} + \boldsymbol{a}_p \tag{3.6b}$$

$$\frac{dm}{dt} = -\frac{T}{c} \tag{3.6c}$$

26

where equations (3.6a) and (3.6b) describe how the SC's position and velocity change over time, repectively. Equation (3.6c) represents the decrease in mass due to propellant expenditures. The term $\boldsymbol{g}$ is the gravitational acceleration:

$$\boldsymbol{g} = -\frac{\mu}{r^2}\frac{\boldsymbol{r}}{r} \tag{3.7}$$

where μ is the gravitational parameter of the central body and $\boldsymbol{r}$ is the vector connecting the centers of mass of the two bodies.

3.3.1 Assumptions for the Two-Body Equation

To derive the two-body equation, we make several assumptions:

- The mass of the satellite is negligible compared to the mass of the attracting body, which is often the case for artificial satellites;

- The chosen coordinate system is inertial, which simplifies the calculations by removing derivatives of the coordinate system itself;

- Both the satellite and the attracting body are assumed to be spherically symmetric with uniform density, allowing them to be treated as point masses;

- The only forces considered are gravitational forces acting along the line joining the centers of the two bodies.

For two-body motion, these assumptions are the defining statements, but, as later sections will describe, perturbations significantly change the orbit and can't be ignored for real-world simulations. These hypotheses leave us with the basic two-body equation, which is derived directly from Newton's law of gravitation.

$$\ddot{\boldsymbol{r}} = -\frac{\mu}{r^2}\frac{\boldsymbol{r}}{r} \tag{3.8}$$

Two useful quantities result from this simplification: specific angular momentum and specific mechanical energy, and it can be demonstrated that both of these are constant along any given orbit. The conservation of the specific angular momentum:

$$\boldsymbol{h} = \boldsymbol{r} \times \boldsymbol{v} = cost \tag{3.9}$$

implies that, for two body motion, the satellite's orbit is always confined to the plane of the orbit. Any position and velocity pair taken at the same point in time uniquely determines the specific angular momentum of the orbit.

Specific mechanical energy is composed of two terms, the first represents the specific kinetic energy, while the second refers to the specific potential energy:

$$\mathscr{E} = \frac{V^2}{2} - \frac{\mu}{r} = c \tag{3.10}$$

where c is a constant and its value is arbitrary, which allows to designate the condition for $\mathscr{E} = 0$ which in space mechanics occurs with a parabolic trajectory. The transition from negative to positive values of E distinguishes closed orbits (ellipses, $\mathscr{E} < 0$) from open orbits ($\mathscr{E} \geq 0$, for parabolas ($=$) and hyperbolae ($>$)).

The application of two-body dynamics requires the definition of Sphere of Influence (SOI). Although the SOI has characteristic shapes depending on the complex interaction among other gravitational bodies, under suitable simplifying assumptions it can be considered a perfect sphere surrounding the central body, within which the gravitational pull of that body dominates all orbital motion. Beyond this sphere, the gravitational influence of other bodies becomes more significant and affects the trajectory of the satellite to a greater extent. The sphere's radius is approximately equal to:

$$r_{SOI,ij} \approx r_{ij} \left(\frac{m_j}{m_i} \right)^{2/5} \tag{3.11}$$

where $\boldsymbol{r}_{ij} = \boldsymbol{r}_j - \boldsymbol{r}_i$ is the position vector of the smaller j-th gravitational body with respect to the bigger i-th gravitational body.

As long as the optimization tool is concerned, a simple 2BP was implemented to allow for easier convergence and faster computation time. This choice is justified by the order of magnitude of the accelerations involved in the LEO environment: Earth's gravitational pull is by far the strongest, with an order of magnitude between 1×10^{-2} and 1×10^{-3}km/s, whilst other celestial bodies like the Sun and Moon cause accelerations of around 1×10^{-9} km/s. Drag is the strongest perturbation at lower altitudes but is highly dependant on the analyzed object's attitude and consequent reference surface, with accelerations varying between 1×10^{-5} and 1×10^{-12} km/s within the first km above Earth surface. Earth oblateness, represented by the J_2 coefficient causes a deviation of the gravitational field of Earth from perfect sphere with an acceleration of around 1×10^{-5}. In first approximation and with restrained propagation times it is possible to neglect these perturbations. On the other hand, high-fidelity propagation is needed to obtain reliable ephemerides for accurate computations of the Probability of Collision (PoC) between two orbiting objects. Therefore, a more complicated dynamic model was implemented in the collision risk evaluation tool. The perturbations considered in the model are presented in the next section.

3.4 Perturbing accelerations

The dynamical model employed in the propagation tool developed for this thesis incorporates the four main perturbing effects experienced by an orbiting object in a LEO trajectory: Earth's asphericity, atmospheric drag, solar radiation pressure

and lunisolar effect. These perturbations were identified as the most significant in a LEO environment and, combined, they constitute the cumulative perturbing acceleration found in the system of equations (3.6b).

$$\boldsymbol{a}_p = \boldsymbol{a}_J + \boldsymbol{a}_D + \boldsymbol{a}_{SRP} + \boldsymbol{a}_{3B} \tag{3.12}$$

The following sections present a detailed discussion of each perturbation, accompanied by a comprehensive account of the modeling techniques employed.

3.4.1 Earth asphericity

The irregular shape of the Earth gives rise to gravitational anomalies across its surface, which in turn affect the gravitational attraction experienced by orbiting objects. These anomalies are primarily the result of the centrifugal force generated by the Earth's rotation, which causes the equatorial regions to bulge outward, giving the Earth a slightly oblate shape. This asymmetry is a significant contributor to variations in the gravitational field, which in turn perturb the orbits of satellites and other objects. Furthermore, areas of higher mass concentration, such as mountains or dense rock formations, exert slightly stronger gravitational forces than regions with lower mass concentration, such as ocean basins or valleys. These variations in gravitational attraction contribute to additional perturbations in the trajectories of orbiting objects.

Given that the gradient of the potential for a central body yields the acceleration, it is possible to form a potential function that includes the perturbing accelerations due to a nonspherical central body, for further details please refer to [10]. The dimensional aspherical potential $\mathscr{U}$ of an object positioned at geocentric distance r, with longitude θ_{LO} ans latitude φ can be expressed as:

$$
\begin{aligned}
\mathscr{U} = \frac{\mu}{r} \Big\{ 1 - \sum_{l=2}^{\infty} J_l \left(\frac{R_\oplus}{r} \right)^l P_l[\sin(\varphi)] + \\
+ \sum_{l=2}^{\infty} \sum_{m=1}^{l} \left(\frac{R_\oplus}{r} \right)^l P_{l,m}[\sin(\varphi)][C_{l,m} \cos(m\theta_{LO}) + S_{l,m} \sin(m\theta_{LO})] \Big\}
\end{aligned}
\tag{3.13}
$$

where $P_{l,m}$ are the associated Legendre polynomials, and $C_{l,m}$ and $S_{l,m}$ are the spherical harmonic coefficients. This form highlights the different contributions to the potential from zonal and tesseral terms:

- Zonal harmonics are defined by the zeroth order ($m = 0$) and are accounted for in the first term of equation (3.13). As can be seen, this term lacks dependency on longitude, indicating that the field is symmetrical about the polar axis. They represent bands of latitude. The term J_2 ($l = 2, m = 0$) is the most significant contributor to the gravitational departure of Earth from a perfect sphere, accounting for the majority of the planet's oblateness [10].

- Tesseral harmonics are a subset of harmonics that account for cases where $l \neq m \neq 0$. They are represented by the second term in equation (3.13). Their purpose is to model specific regions on Earth that deviate from a perfect sphere. The case of $l = m$ defines sectoral harmonics, which represent bands of longitude [10].

In order to retrieve the most accurate spherical harmonic coefficients the Earth Gravitational Model 2008 (EGM2008) was implemented in the Python tool developed for this work. Extensive details regarding this model can be found in [11].

As mentioned, equation (3.13) needs the terrestrial longitude, which is the angle between $\hat{\boldsymbol{X}}$ and the spacecraft's projected position on the ITRF93's reference plane. To obtain θ_{LO} the following relation can be exploited:

$$\theta_{LO}(t) = \theta_{ijk} - \theta_{G_{ijk}}(t) = \theta_{ijk} - [\theta_{Gref_{ijk}} + w_\oplus(t - t_{ref})] \qquad (3.14)$$

where t_{ref} is the J2000 epoch, January 1st, 2000 at 12:00:00 UTC, and $\theta_{Gref_{ijk}} = 280.46061837504deg$ is the longitude of the prime meridian in the J2000 RF at that epoch. $w_\oplus$ is evaluated assuming the sidereal day equal to $86164.098903690351s$ (precession is neglected).

Accelerations caused by Earth's irregular gravitational field are obtained by calculating the gradient of the potential function. In order to compute the perturbations that deviate Earth's potential function from that of a sphere (μ_E/r), the function that is partially derived is $\Phi = \mathscr{U} + \mu_E/r$; in the ZEN RF:

$$(a_J)_u = \frac{\partial \Phi}{\partial r} \qquad (3.15a)$$

$$(a_J)_v = \frac{\partial \Phi}{\partial \theta} \frac{1}{r \cos \varphi} \qquad (3.15b)$$

$$(a_J)_w = \frac{\partial \Phi}{\partial \varphi} \frac{1}{r} \qquad (3.15c)$$

The calculation of derivatives with respect to r and θ is relatively straightforward; on the contrary, derivatives with respect to φ, involve the computation of the derivatives of the associated Legendre functions. These derivatives are obtained recursively, exploiting the characteristics of Legendre polynomials.

In first analysis, greater propagation performances with an acceptable degree of fidelity can be achieved by considering the sole J_2 perturbation. This case involves only one associated Legendre function, $P_{2,0}$:

$$P_{2,0} = \frac{1}{2}[3\sin^2(\varphi) - 1] \qquad (3.16)$$

Perturbing accelerations can be easily obtained:

$$(a_J)_u = \frac{\mu}{r^2}\{J_2\left(\frac{R_\oplus}{r}\right)^2 \frac{1}{2}[3\sin^2(\varphi) - 1]\} + \frac{\mu}{r}\{J_2\left(\frac{R_\oplus^2}{r^3}\right)[3\sin^2(\varphi) - 1]\} \quad (3.17a)$$

$$(a_J)_v = 0 \quad (3.17b)$$

$$(a_J)_w = -\frac{\mu}{r^2}\{J_2\left(\frac{R_\oplus}{r}\right)^2 3\sin(\varphi)\cos(\varphi)\} \quad (3.17c)$$

3.4.2 Atmospheric Drag

Although the atmosphere is quite rarefied in its upper layers, it still has a low density of molecules that, when colliding with an orbiting object, provide a drag force that is non-negligible for high-fidelity LEO modeling. As a matter of fact, next to the oblateness of the Earth, atmospheric drag most strongly influences the motion of a satellite near Earth, and during the last few revolutions of a satellite's life, drag effects can be more dominant than J2 effects [10]. Being a velocity-dependent perturbation, drag force is nonconservative and changes the total energy of the orbit, lowering it. Drag changes mainly the semimajor axis and eccentricity of the orbit. Acceleration due to drag can be expressed with the following, well known equation:

$$\boldsymbol{a}_D = -\frac{1}{2}\frac{C_D A}{m}\rho v_{rel}^2 \frac{\boldsymbol{v}_{rel}}{|\boldsymbol{v}_{rel}|} \quad (3.18)$$

where C_D is the drag coefficient, A and m are the spacecraft's exposed cross-sectional area and mass respectively, and v_{rel} is the relative velocity between the spacecraft and the atmosphere.

- the drag coefficient is a dimensionless quantity that reflects the satellite's susceptibility to drag forces. For satellites in the upper atmosphere it is usually approximated to 2.2 (using a flat plate model). Spheres have $C_D \approx 2.0$ to 2.1. The drag coefficient is satellite configuration-specific and is seldom approximated to more than three significant digits [10];

- the cross-sectional area of the spacecraft exposed to the relative velocity is dependent on spacecraft attitude, in first analysis it will be approximated to a constant value. Usually $m/(C_D A)$ is referred to as *ballistic coefficient, BC* which is another measure of a satellite's susceptibility to drag effects [10];

- the atmospheric density, ρ, is a crucial parameter, since its value, in addition to altitude, is strongly influenced by Earth's magnetic field and solar activity and can vary by orders of magnitude. To properly estimate the atmosphere's density

at relevant positions and epochs the MSIS (Mass Spectrometer and Incoherent Scatter Radar) atmospheric model was implemented in the developed tool. The MSIS model is based on empirical formulations derived from observational data collected by various instruments such as mass spectrometers and incoherent scatter radars. For more specific information regarding this model please refer to [12].

- The velocity is *not* the velocity vector found in the state vector, but it's relative to the atmosphere, which has a mean motion due to Earth's rotation:

$$\boldsymbol{v}_{rel,ijk} = \boldsymbol{v}_{sc,ijk} - \boldsymbol{w}_{\oplus} \times \boldsymbol{r}_{ijk} \tag{3.19}$$

3.4.3 Solar Radiation Pressure

Like drag, solar radiation pressure is a non-conservative disturbance but becomes more pronounced at higher altitudes. One of the most difficult aspects of solar radiation analysis is accurately modeling and predicting solar cycles and variations. Because this disturbance has a lesser effect on orbiting objects at the altitudes of interest for this work, an average energy of incoming solar radiation is considered. The *solar-radiation constant*, or solar flux, SF, is:

$$SF = 1367 \quad W/m^2 \tag{3.20}$$

Using Einstein's law relating energy with mass, $E = mc^2$, with c being the speed of light, it is possible to find the force of solar pressure per unit area, p_{srp}, which is equal to the change in the momentum imparted to the object of mass m:

$$p_{srp} = mc = \frac{E}{c} = \frac{1367}{3 \times 10^8} = 4.5567 \times 10^{-6} \quad \frac{N}{m^2} \tag{3.21}$$

By introducing the *reflectivity*, C_R, and the exposed area to the sun $A_{\odot}$, it is now possible to define the force of the solar radiation pressure [10]:

$$\boldsymbol{F}_{SRP} = -p_{srp} C_R A_{\odot} \frac{\boldsymbol{r}_{sc\odot}}{|\boldsymbol{r}_{sc\odot}|} \tag{3.22}$$

where:

- $\boldsymbol{r}_{sc\odot}$ is the J2000 position vector of the Sun with respect to spacecraf;

- the reflectivity, C_R, is value between 0.0 and 2.0 that indicates how the satellite reflects the incoming radiation. A value of 0.0 means the object is transluscent to incoming radiation: no momentum is transmitted. A value of 1.0 means that all the radiation is absorbed (black body), and all the momentum is transmitted, resulting in perturbing force. A value of 2.0 indicates that all the

radoation is reflected and twice the momentum is transmitted, which is the case for a flat mirror perpendicular to the light source [10]. As it is for the drag coefficient, the reflectivity is a satellite configuration-specific parameter and depends on spacecraft attitude and light conditions, in this work it will be approximated to a constant value;

- much like it is for the cross sectional area considered in the computation of drag forces, the exposed area to the sun $A_\odot$ is dependent on spacecraft attitude and is here approximated to a constant value.

Newton's second law allows us to determine the acceleration experienced by an object of mass m irradiated by the Sun:

$$\boldsymbol{a}_{SRP} = \frac{\boldsymbol{F}_{SRP}}{m} = -\frac{p_{srp}C_R A_\odot}{m}\frac{\boldsymbol{r}_{sc\odot}}{|\boldsymbol{r}_{sc\odot}|} \qquad (3.23)$$

Once again, a coordinate transformation is needed to obtain the acceleration components in the ZEN RF.

The modeling of this disturbance is inevitably correlated to the illumination conditions of the spacecraft. Unless following a dusk-to-dawn orbit, the object of interest will experience periods of partial and total eclipse, penumbra and umbra respecively, determined mainly by the shadowing of the Sun caused by Earth. During umbra conditions the SRP perturbing acceleration is null, while during penumbra it is proportional to the fraction of solar radiation that is still able to reach the spacecraft.
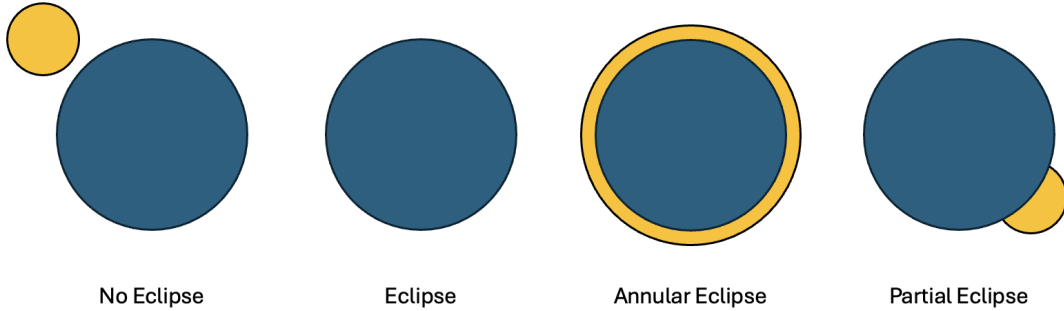

No Eclipse   Eclipse   Annular Eclipse   Partial Eclipse

Figure 3.2: Light conditions to be evaluated

To assess these cases, it is necessary to evaluate the apparent size of the relevant celestial bodies, as seen from the spacecraft, $\theta_\odot$ and $\theta_\oplus$, along with the angular

separation between them γ, [13].

$$\theta_{\odot} = \arcsin\left(\frac{R_{\odot}}{r_{sc\odot}}\right) \tag{3.24a}$$

$$\theta_{\oplus} = \arcsin\left(\frac{R_{\oplus}}{r_{sc\oplus}}\right) \tag{3.24b}$$

$$\gamma = \arccos\left(\frac{\boldsymbol{r}_{sc\odot} \cdot \boldsymbol{r}_{sc\oplus}}{r_{sc\odot}r_{sc\oplus}}\right) \tag{3.24c}$$

The function L, which assesses the light conditions experimented by the satellite, is now introduced:

$$L = \begin{cases} 1 & if \quad \gamma - \theta_{\odot} > \theta_{\oplus} \\ 0 & if \quad \theta_{\oplus} > \gamma + \theta_{\odot} \\ 1 - \frac{\theta_{\oplus}^2}{\theta_{\odot}^2} & if \quad \theta_{\odot} - \theta_{\oplus} \geq \gamma \quad or \quad \gamma \geq \theta_{\odot} + \theta_{\oplus} \\ 1 - \frac{A+B-C}{\pi\theta_{\odot}^2} & else \end{cases} \tag{3.25}$$

where:

$$A = \theta_{\oplus}^2 \arccos\left(\frac{\gamma^2 + \theta_{\oplus}^2 - \theta_{\odot}^2}{2\gamma\theta_{\oplus}}\right) \tag{3.26a}$$

$$B = \theta_{\odot}^2 \arccos\left(\frac{\gamma^2 + \theta_{\odot}^2 - \theta_{\oplus}^2}{2\gamma\theta_{\oplus}}\right) \tag{3.26b}$$

$$C = \frac{1}{2}\sqrt{(-\gamma + \theta_{\oplus} + \theta_{\odot})(\gamma + \theta_{\oplus} - \theta_{\odot})(\gamma - \theta_{\oplus} + \theta_{\odot})(\gamma + \theta_{\oplus} + \theta_{\odot})} \tag{3.26c}$$

L needs to be multiplied to $\boldsymbol{a}_{SRP}$ from equation (3.23) to obtain the true perturbative accelerations caused by solar radiation along the satellite's trajectory, [14]. The Sun's position with respect to Earth and to the orbiting object is retrieved from DE440 JPL ephemerides.

3.4.4 Lunisolar Effect

Third bodies, such as the Moon and the Sun, have small perturbing effects in lower orbits, but are still considered in the dynamic model to ensure high-fidelity orbit propagation. The contribution of the *i-th* body is modeled as:

$$a_{3Bi} = \mu_i\left(\frac{\boldsymbol{r}_{sat-i}}{r_{sat-i}^3} - \frac{\boldsymbol{r_i}}{r_i^3}\right) \tag{3.27}$$

where μ_i is the gravitational parameter of the *i-th* body, $\boldsymbol{r}_{sat-i}$ is the position vector of the satellite relative to the *i-th* body, and $\boldsymbol{r_i}$ is the position vector of the *i-th* body relative to Earth.

Two terms can be distinguished in expression (3.27):

- the first contribute is called *direct effect* and represents the acceleraration that the third body induces on the object of interest;

- the second term is reffered to as *indirect effect* since it models the acceleration that the third body induces on the central body, in this case Earth.

Chapter 4

Close Approach Analyis

"Close Approach" refers to the moment when two spacecraft are at their closest point to each other. The importance of accurately analyzing these conditions, known as "Conjunction Assessment," is underscored by events like the 2009 Iridium-33/Cosmos-2251 collision, which generated a substantial amount of additional orbital debris endangering satellite operations in LEO. The need to consider collision avoidance as part of routine operations is evident to all mission operators and should also be seen as good practice in view of space debris mitigation. Since May 2004, the Center for Space Standards and Innovation (CSSI) has been issuing daily reports on potential conjunctions within a 5 km distance threshold for the upcoming week. These reports cover all objects in Earth orbit using the complete catalog of unclassified NORAD Two-Line Elements (TLEs) available to the public. This program is known as Satellite Orbital Conjunction Reports Assessing Threatening Encounters in Space (SOCRATES) [15]. Via STK's Conjunction Analysis Tool, SOCRATES is able to provide reports on both minimum distance and maximum probability for the conjunction. The developed tool for this thesis implements a simplified version of a method developed by Alfano and Negron, called the *Alfano-Negron Close Approach Software (ANCAS)*. This method provides close approach data between two arbitrary, non-maneuvering spacecrafts, and is here simplified by lacking covariance information, since this topic wasn't the focus of this work. Insights on the method are provided in section 4.2, for further information please refer to [10].

4.1 Apogee-Perigee Filter

A first screening filter was implemented to reduce the computational burden where it is not needed: a simple comparison between apogee and perigee values of the orbits provides a rapid estimation to determine if close approaches are possible.

If the absolute value between the largest perigee, r_{pmax}, and the smallest apogee r_{amin}, is greater than a threshold distance, the two objects will not come close enough to require a full conjunction assessment:

$$if: \quad |r_{pmax} - r_{amin}| > TD, \quad then: \quad \text{no conjunction} \tag{4.1}$$

Spacecrafts that pass this initial test do not require any further processing.

4.2 Miss Distance Determination

As previously mentioned, the Probability of Collision estimation tool exploits a high fidelity propagator to obtain accurate orbit data for the two objects of interests and the ANCAS method to perform the conjunction assessment. ANCAS has several advantages over traditional, brute force, methods, like sequencially stepping along the orbits of the two satellites:

- it uses a relative-distance function for which each point and slope matches in the blending functions;

- the method may use any propagation scheme;

- the results are obtained from a closed-form solution and eliminate the need for iteration.

In the context of this chapter the two objects being observed for conjunction assessment will be reffered to as "primary" and "secondary" satellites, where the primary satellite is the maneuvering spacecraft in case collision avoidance is deemed necessary and the secondary object represents either an active or passive satellite or orbital debris.

From the propagated trajectories, the J2000 positions of the primary and secondary satellites, respectively $\boldsymbol{r}_p$ and $\boldsymbol{r}_s$, are used to obtain the relative-distance vector, $\boldsymbol{r}_d$ and its time derivatives:

$$\boldsymbol{r}_d = \boldsymbol{r}_s - \boldsymbol{r}_p \tag{4.2a}$$

$$\dot{\boldsymbol{r}}_d = \dot{\boldsymbol{r}}_s - \dot{\boldsymbol{r}}_p \tag{4.2b}$$

$$\ddot{\boldsymbol{r}}_d = \ddot{\boldsymbol{r}}_s - \ddot{\boldsymbol{r}}_p \tag{4.2c}$$

Since a splining technique is implemented in this method, large time steps are allowed for the propagation, ensuring lower computation times. Now it is possible

to define the distance function, $f_d(t)$, and its time derivatives:

$$f_d(t) = \boldsymbol{r}_d \cdot \boldsymbol{r}_d \tag{4.3a}$$

$$\dot{f}_d(t) = 2(\dot{\boldsymbol{r}}_d \cdot \boldsymbol{r}_d) \tag{4.3b}$$

$$\ddot{f}_d(t) = 2(\ddot{\boldsymbol{r}}_d \cdot \boldsymbol{r}_d + \dot{\boldsymbol{r}}_d \cdot \dot{\boldsymbol{r}}_d) \tag{4.3c}$$

Close approach conditions verify when the distance function is at a local minimum, which is when $\dot{f}_d(t) = 0$ and $\ddot{f}_d(t) > 0$, where the second condition ensures that the two objects are in the same half-plane of the orbit. Cubic splining in each integration time interval is exploited to find the times of closest approach: given the distance function and its time derivatives at the beginning and end of each time interval, t_n and t_{n+1} respectively, the cubic polynomial $P_c(\tau)$ is defined as:

$$P_c(\tau) = \alpha_{c3}\tau^3 + \alpha_{c2}\tau^2 + \alpha_{c1}\tau + \alpha_{c0} \tag{4.4}$$

where τ is a normalized time variable and uniformly spans the interval ($0.0 < \tau < 1.0$) and the α_c coefficients are defined as follows:

$$\alpha_{c0} = \dot{f}_d(t_n) \tag{4.5a}$$

$$\alpha_{c1} = \ddot{f}_d(t_n)\Delta t \tag{4.5b}$$

$$\alpha_{c2} = -3\dot{f}_d(t_n) - 2\ddot{f}_d(t_n)\Delta t + 3\dot{f}_d(t_{n+1}) - \ddot{f}_d(t_{n+1})\Delta t \tag{4.5c}$$

$$\alpha_{c3} = 2\dot{f}_d(t_n) + \ddot{f}_d(t_n)\Delta t - 2\dot{f}_d(t_{n+1}) + \ddot{f}_d(t_{n+1})\Delta t \tag{4.5d}$$

with $\Delta t = t_{n+1} - t_n, \quad t_{n+1} > t_n$.
If:

$$\frac{dP_c(\tau)}{d\tau} > 0 \quad at \quad \tau = \tau_{root} \tag{4.6}$$

a local minimum distance exists.
Now, using quintic splining, it is possible to account for the contribute of acceleration and determine the distance at τ_{root}. Three quintics must be solved (one for each axis), with the quintic polynomial $P_q(\tau)$ being:

$$P_{qi}(\tau) = \alpha_{q5i}\tau^5 + \alpha_{q4i}\tau^4 + \alpha_{q3i}\tau^3 + \alpha_{q2i}\tau^2 + \alpha_{q1i}\tau + \alpha_{q0i} \tag{4.7}$$

with $i = \{I, J, K\}$ and the α_{qi} defined as:

$$\alpha_{q0i} = r_{di}(t_n) \tag{4.8a}$$

$$\alpha_{q1i} = \dot{r}_{di}(t_n)\Delta t \tag{4.8b}$$

$$\alpha_{q2i} = 0.5\ddot{r}_{di}(t_n)\Delta t^2 \tag{4.8c}$$

$$\begin{aligned} \alpha_{q3i} = {}&-10r_{di}(t_n) - 6\dot{r}_{di}(t_n)\Delta t - 1.5\ddot{r}_{di}(t_n)\Delta t^2 \\ &+ 10r_{di}(t_{n+1}) - 4\dot{r}_{di}(t_{n+1})\Delta t + 0.5\ddot{r}_{di}(t_{n+1})\Delta t^2 \end{aligned} \tag{4.8d}$$

$$\begin{aligned} \alpha_{q4i} = {}&15r_{di}(t_n) + 8\dot{r}_{di}(t_n)\Delta t + 1.5\ddot{r}_{di}(t_n)\Delta t^2 \\ &- 15r_{di}(t_{n+1}) + 7\dot{r}_{di}(t_{n+1})\Delta t - \ddot{r}_{di}(t_{n+1})\Delta t^2 \end{aligned} \tag{4.8e}$$

$$\begin{aligned} \alpha_{q5i} = {}&-6r_{di}(t_n) - 3\dot{r}_{di}(t_n)\Delta t - 0.5\ddot{r}_{di}(t_n)\Delta t^2 \\ &+ 6r_{di}(t_{n+1}) - 3\dot{r}_{di}(t_{n+1})\Delta t + 0.5\ddot{r}_{di}(t_{n+1})\Delta t^2 \end{aligned} \tag{4.8f}$$

The minimum distance (d_{close} or minimum range) and corresponding time (t_{close} or time at closest approach, TCA) are:

$$d_{close} = \sqrt{P_{qI}^2(\tau_{root}) + P_{qJ}^2(\tau_{root}) + P_{qK}^2(\tau_{root})} \tag{4.9a}$$

$$t_{close} = t_n + \tau_{root} * \Delta t \tag{4.9b}$$

Since this work was based on the absence of known covariances -the unceranties of the predicted state-, the following computation of the Probability of Collision (PoC) is based on a numerical approximation that provides the worst-case collision potential by finding the combined Gaussian probability density that maximizes collision probability [16].

$$PoC_{max} = \frac{1}{2}\{erf\left[\frac{r+1}{2\sqrt{r}}\sqrt{-ln\left(\frac{1-r}{1+r}\right)}\right] + erf\left[\frac{r-1}{2\sqrt{r}}\sqrt{-ln\left(\frac{1-r}{1+r}\right)}\right]\} \tag{4.10}$$

where *erf* is the error function and r is defined as the combined object radius normalized with respect to the miss distance:

$$r = \frac{r_{obj1} + r_{obj2}}{d_{close}} \tag{4.11}$$

For the purposes of this work, computing the worst-case PoC would be too conservative: by accounting for the worst-case uncertainties on the spacecrafts positions, too large maneuvers would be required to lower the PoC to an acceptable

risk level. Hence, a new Probability of Collision has been created by computing a weighted mean between the worst-case PoC and a linear function representing the best-case PoC, for which the risk is acceptable when the minimum range is greater than the combined object radius and is null for an infinite minimum range. The weights are computed as a function of the time at closest approach (TCA) so that the worst-case probability is progressively heavier the greater the TCA is. The resulting weighted PoC should be solely regarded as a benchmark to assess the efficacy of a collision avoidance maneuver and shouldn't in any case replace the results of a more sophisticated PoC computing method involving covariance matrices. The following is a flowchart showing the main steps of the PoC assessment tool:
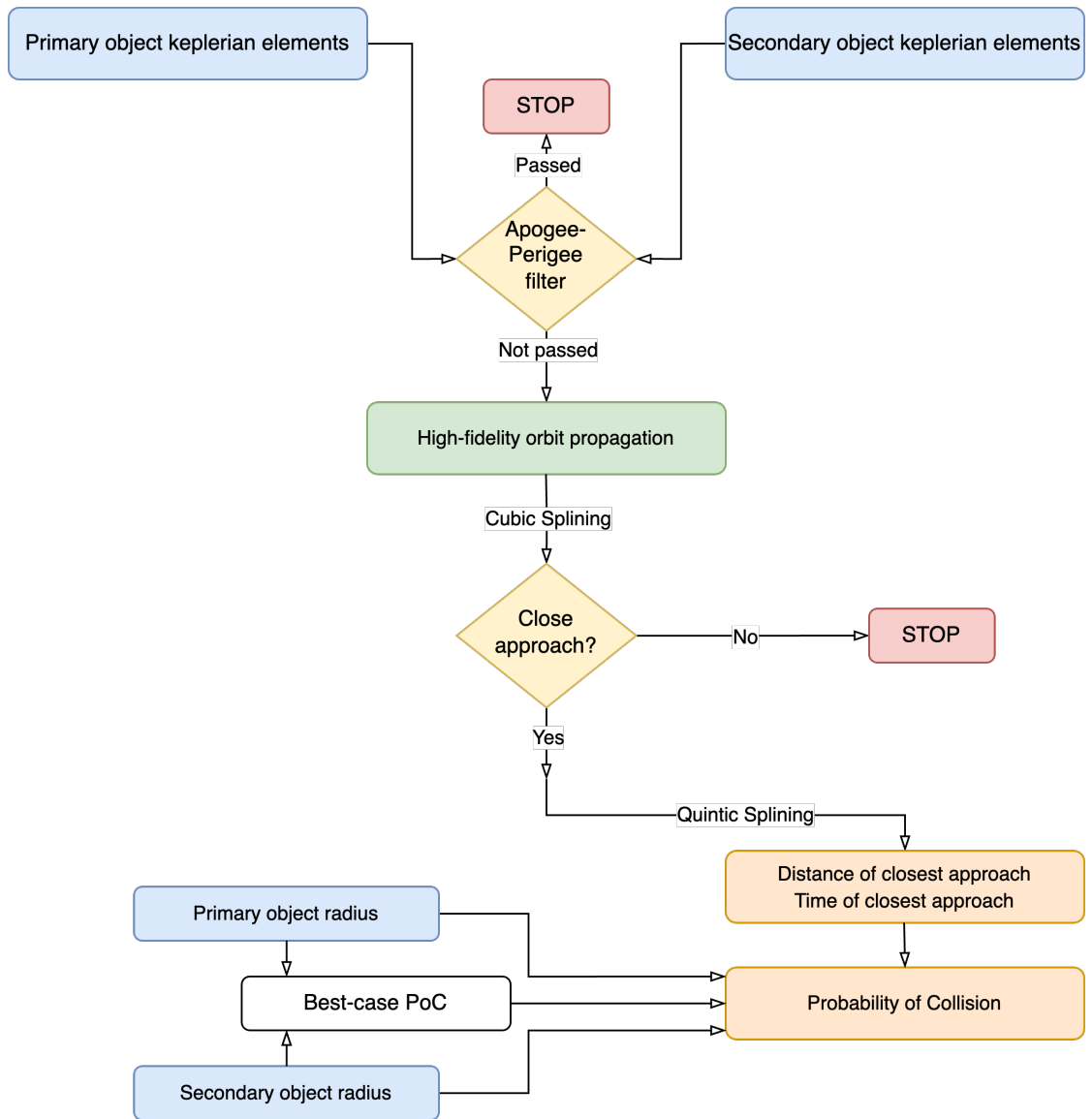
Figure 4.1: PoC computation

4.3   Safety Standards

An essential component of any collision avoidance strategy is the criteria for determining when to execute an avoidance maneuver. The risk threshold that was considered in this work was retrieved from ESA's current collision avoidance strategies. [17] states that a risk threshold of 1×10^{-4} one day to the event leads to a risk reduction of around 90%. Therefore, in this work, an avoidance maneuver

has to be executed whenever the estimated PoC is greater than 1×10^{-4} and should modify the primary spacecraft's semimajor axis enough to guarantee a new PoC lower than 1×10^{-4}. The following flowchart summarises the general steps needed to search for the optimal avoidance maneuver:
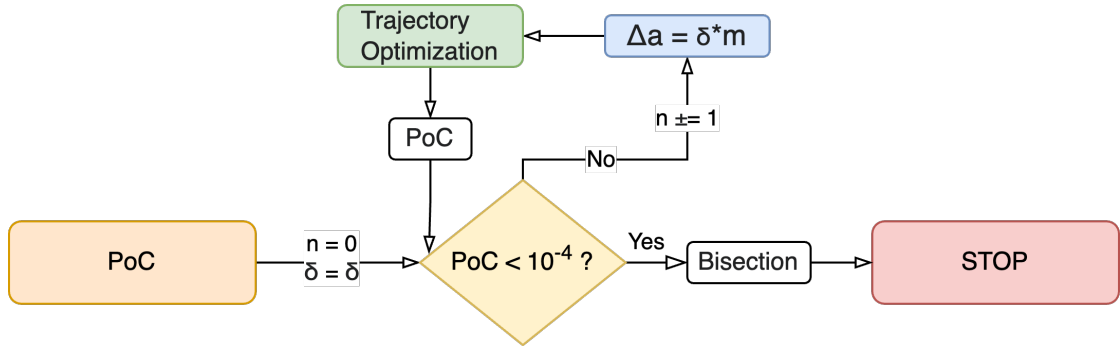
Figure 4.2: Maneuver threshold and general search method for Optimal trajectory

where δ represents a fixed step variation of the target semimajor axis.

In theory, the trajectory of the primary spacecraft must be optimized for each new target orbit in order to determine the object's position and mass at the end of the maneuver. These values must then be entered as new initial conditions in the PoC evaluation tool. This is true if the optimization and PoC dynamic frameworks are identical. In this work's case, however, using the primary object state resulting from a two-body propagation while obtaining the secondary object position with a perturbed propagation would lead to erroneous evaluations of the risk of collision. Given that the trajectories in question require low maneuvering times, it was deemed sufficient to evaluate the resulting PoC by modifying the semimajor axis of the corresponding delta in each iteration. This approach not only ensures the validity of the obtained PoC but also eliminates the need for trajectory optimization on a repeated basis. The workflow of this research project can be schematized as follows:
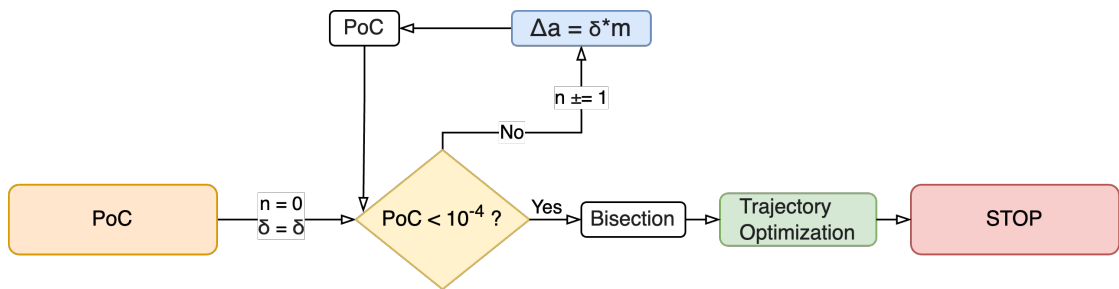
Figure 4.3: Implemented maneuver search

Once a first admissible semimajor axis variation is identified, a bisection approach is employed to reduce the delta interval until a one-meter precision is achieved. Pursuing a precision below this threshold was deemed to be an excessive demand for the purposes of this study, given the approximations made in terms of PoC calculation and optimal trajectory determination.

Chapter 5

The Implemented Optimal Control Problem

This chapter presents an overview of the implemented Boundary Value Problem in section 5.1. Collision avoidance maneuvers (CAMs) could be performed by changing any orbital element of at least one of the colliding objects, but in-track maneuvers are usually the preffered strategy, since a change in the semimajor axis directly affects the radial distance between the satellites and affects the orbital period; the distance at closest approach is increased by the combined effect of these 2 phenomena, while ΔV requirements are minimized. Therefore, Δa maneuvers are investigated, under the hypothesis of a free-attachment orbital insertion, i.e. without specifying an exact target point on the target orbit. Moreover the time needed to perform the maneuver is left as a free variable; more on this is discussed in section 5.1.3. Finally, in section 5.2 an illustrative example is discussed.

5.1   OCP for space trajectory optimization

The Optimal Control Problem applied to the system of ODEs derived for a two-body dynamic model in the Cartesian reference frame (J2000) aims to find the optimal control law $\boldsymbol{T}^*(t)$ that maximizes the final mass of the spacecraft at the

end of the trajectory and is defined as:

$$\text{OCP} = \begin{cases} \max \quad J = m_f \\[2mm] \begin{cases} \dot{\boldsymbol{r}}(t) = \boldsymbol{V}, & t \in [0, t_f] \\[2mm] \dot{\boldsymbol{V}}(t) = -\frac{\mu}{r^3}\boldsymbol{r} + \frac{\boldsymbol{T}}{m(t)}, & t \in [0, t_f] \\[2mm] \dot{m}(t) = -\frac{T}{c}, & t \in [0, t_f] \end{cases} \\[8mm] \text{s.t.} \\[2mm] T \leq T_{\max} \\[2mm] \boldsymbol{r}_i, \boldsymbol{V}_i \leftarrow \text{initial orbit keplerian elements} \\[2mm] \boldsymbol{r}_f, \boldsymbol{V}_f \leftarrow \text{target orbit keplerian elements} \\[2mm] m_i = m_{sc} \\[2mm] t_f = \text{free} \end{cases} \tag{5.1}$$

As already presented in chapter 2, to each state variable is associated a costate, or adjoint, variable. The augmented state vector, or *fullstate*, is defined as:

$$\boldsymbol{fullstate} = \{x, y, z, v_x, v_y, v_z, m, \lambda_x, \lambda_y, \lambda_z, \lambda_{vx}, \lambda_{vy}, \lambda_{vz}, \lambda_m\}$$

$$= \{\boldsymbol{r}, \boldsymbol{V}, m, \boldsymbol{\lambda_r}, \boldsymbol{\lambda_V}, \lambda_m\} = \{\boldsymbol{S}, m, \boldsymbol{C}, \lambda_m\} \tag{5.2a}$$

Now the Hamiltonian for the defined OCP can be obtained:

$$H = \boldsymbol{\lambda}^T \boldsymbol{f} = \boldsymbol{\lambda_r} \cdot \boldsymbol{V} + (\boldsymbol{\lambda_V} \cdot \boldsymbol{r})\frac{-\mu}{r^3} + \boldsymbol{\lambda_V} \cdot \frac{\boldsymbol{T}}{m} - \lambda_m \frac{T}{c} \tag{5.3}$$

5.1.1 Optimal Thrust

The PMP states that the optimal control maximizes the Hamiltonian H in order to maximize the merit index J. As it can be seen from equation (5.3), the optimal thrust direction that maximizes the Hamiltonian is parallel to the adjoint velocity vector, or *primer vector*, $\boldsymbol{\lambda_V}$:

$$\boldsymbol{T} = T\frac{\boldsymbol{\lambda_V}}{\lambda_V} \tag{5.4}$$

where λ_V is the primer vector's module:

$$\lambda_V = \sqrt{\lambda_{vx}^2 + \lambda_{vy}^2 + \lambda_{vz}^2} \tag{5.5}$$

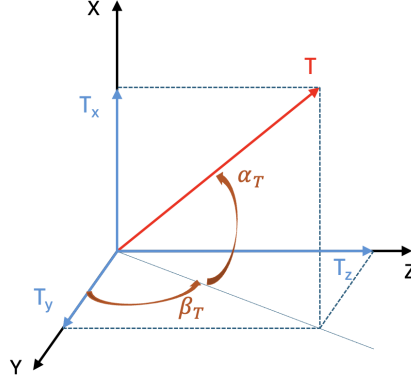The thrust vector can be decomposed as follows:

Figure 5.1: Thrust angles in the cartesian RF

with:

$$\begin{cases} T_x = T \sin \alpha_T \\ T_y = T \cos \alpha_T \cos \beta_T \\ T_z = T \cos \alpha_T \sin \beta_T \end{cases} \tag{5.6}$$

Hence, the thrust angles α_T and β_T can be expressed in terms of the velocity costates:

$$\sin \alpha_T = \frac{\lambda_{vx}}{\lambda_V} \tag{5.7a}$$

$$\cos \alpha_T cos \beta_T = \frac{\lambda_{vy}}{\lambda_V} \tag{5.7b}$$

$$\cos \alpha_T sin \beta_T = \frac{\lambda_{vz}}{\lambda_V} \tag{5.7c}$$

By grouping the terms that contain the control variable T in equation (5.3), the Hamiltonian can be re-written by highlighting the switching function, SF:

$$H = \boldsymbol{\lambda_r} \cdot \boldsymbol{V} + (\boldsymbol{\lambda_V} \cdot \boldsymbol{r})\frac{-\mu}{r^3} + T SF \tag{5.8a}$$

$$SF = \frac{\lambda_V}{m} - \frac{\lambda_m}{c} \tag{5.8b}$$

From equation (5.8a) it is clear that the Hamiltonian is linear with the control, hence a bang-bang control law arises, and that the optimal thrust magnitude is

maximized when its multiplier, the switching function, is positive, and is minimized when the SF is negative:

$$T = \begin{cases} T_{\max}, & \text{if } SF > 0 \\ 0, & \text{if } SF < 0 \end{cases} \tag{5.9}$$

5.1.2 Euler-Lagrange Equations

The ODEs for the costate variables are obtained via the partial derivation of the Hamiltonian with respect to the corresponding state variables, with a minus sign; the resulting vectorial equations are here reported:

$$\frac{d\boldsymbol{\lambda_r}}{dt} = -\frac{\partial \boldsymbol{g}}{\partial \boldsymbol{r}} \cdot \boldsymbol{\lambda_V} \tag{5.10a}$$

$$\frac{d\boldsymbol{\lambda_V}}{dt} = -\boldsymbol{\lambda_r} \tag{5.10b}$$

$$\frac{d\lambda_m}{dt} = \frac{T}{m^2}\lambda_V \tag{5.10c}$$

where in equation (5.10a) $\boldsymbol{g} = -\frac{\mu}{r^3}\boldsymbol{r}$.

5.1.3 Terminal Conditions

As mentioned at the beginning of this chapter, the maneuver of choice in this work is a *free-time*, *free-attachment* orbital insertion. A *free-attachment* orbital insertion doesn't specify the insertion point on the final orbit, leaving the final true anomaly as a free variable, to be determined by the optimal solution. For this purpose, the reduced transversality conditions described in [18] were exploited to obtain a condition that accounts for the added degree of freedom of the true anomaly.

Reduced Transversality Conditions:
The reduced transversality conditions are analogous to the transversality conditions, here referred to as "optimality conditions", for the same OCP, with the variables in the terminal constraints replaced by the orbital elements. The keplerian orbital element vector is referred to as $\boldsymbol{K}$:

$$\boldsymbol{K} = [a, e, i, \Omega, \omega, \nu] \in R^6 \tag{5.11}$$

Let K_i be a free element that does not appear in any constraint, in this case $K_i = \nu$, in general, at t_f:

$$\frac{\partial \boldsymbol{\psi}}{\partial K_i} = \frac{\partial \boldsymbol{\psi}(\boldsymbol{S_f})}{\partial \boldsymbol{S_f}}\frac{\partial \boldsymbol{S_f}}{\partial K_i} = 0, \quad i \in I \tag{5.12}$$

where I is the set of indices of the K_i free elements, $\boldsymbol{\psi}$ is the constraints vector, and $\boldsymbol{S}_f$ is the final state obtained from the keplerian orbital element vector. The optimality conditions in equation 2.11d:

$$\boldsymbol{C}_f = \boldsymbol{\mu}^T \frac{\partial \boldsymbol{\psi}}{\boldsymbol{S}_f} \tag{5.13}$$

are modified through the introduction of the $\boldsymbol{y}$ vector, y_i (with $i = 1, \ldots, n \quad n =$ number of free K) being a set of linearly independent solutions to the system:

$$\left(\frac{\partial \boldsymbol{\psi}(\boldsymbol{S}_f)}{\partial \boldsymbol{S}_f} \right) \boldsymbol{y} = 0 \tag{5.14}$$

so that the optimality conditions (5.13) can be replaced by:

$$\boldsymbol{y}(\boldsymbol{x}_f) \cdot \boldsymbol{C}_f = 0 \tag{5.15}$$

From the analogy between expressions (5.12) and (5.14), one can obtain the $(6 - n)$ reduced transversality conditions:

$$\frac{\partial \boldsymbol{S}_f}{\partial K_i} \cdot \boldsymbol{C}_f = 0 \tag{5.16}$$

A solution for a *free-time*, *free-attachment* orbital insertion must include the seven initial costates, the time to maneuver and the final true anomaly. Nine total unknowns require 9 boundary conditions, which are here presented:

- **Maximum final mass:**
  from the optimality condition in equation (2.11d):

$$\lambda_{mf} = 1 \tag{5.17}$$

- **Free-time:**
  from the transversality conditions in equation (2.11b):

$$H_f = 0 \tag{5.18}$$

- **Free-attachment:**
  from the reduced transversality conditions, (5.16):

$$\boldsymbol{V}_f \cdot \boldsymbol{\lambda_{rf}} - \frac{\mu}{r_f^3} \boldsymbol{r}_f \cdot \boldsymbol{\lambda_{Vf}} = 0 \tag{5.19}$$

- **Final state BCs:**

$$\boldsymbol{r}_f = \boldsymbol{r}_f^* \tag{5.20a}$$

$$\boldsymbol{V}_f = \boldsymbol{V}_f^* \tag{5.20b}$$

where $\boldsymbol{r}_f^*$ and $\boldsymbol{V}_f^*$ represent the final desired state, which is obtained by updating the required final keplerian elements with a new final true anomaly in every new iteration.
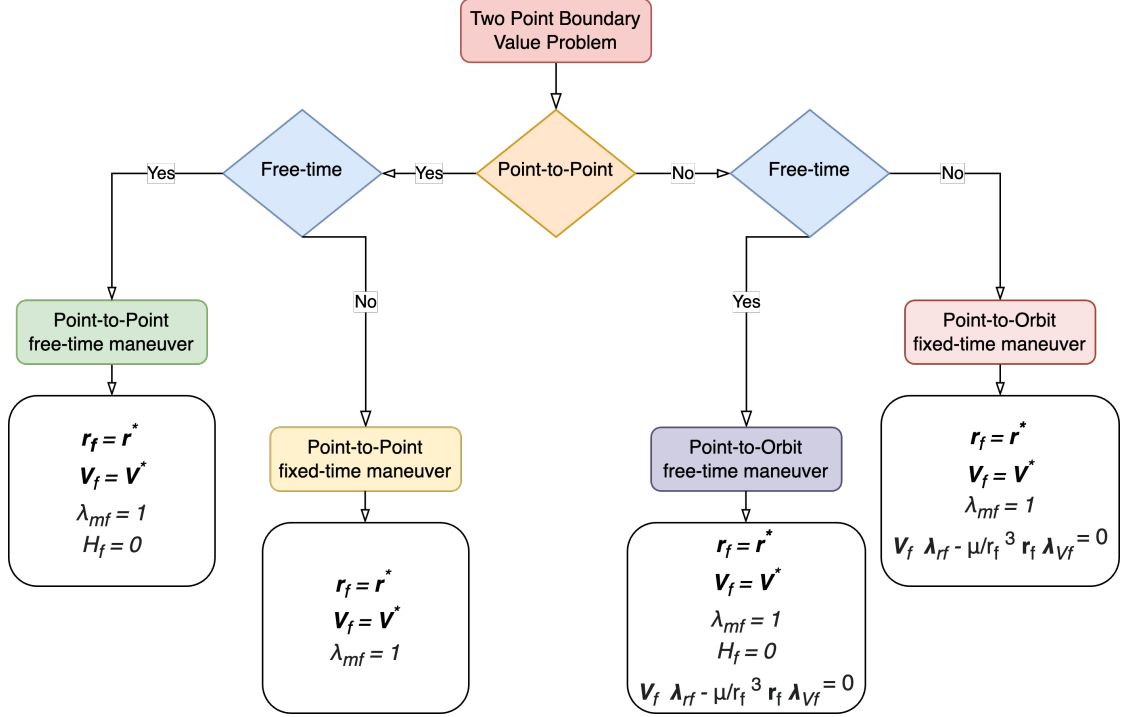

Figure 5.2: TPBVP implemented cases

5.2 An Illustrative Example: LEO orbital insertion

In this example a medium-sized satellite with the following characteristics:

S/C mass	I_{sp}	T
600 kg	3000 s	0.5 N

Table 5.1: Example spacecraft

will be performing an orbital transfer between two circular orbits with the following keplerian parameters:

49

Orbit	a [km]	e	i [deg]	Ω [deg]	ω [deg]	ν [deg]
Initial	$R_e + 450$	0.00	0.00	0.00	0.00	0.00
Target	$R_e + 460$	0.00	0.01	0.00	0.00	free

Table 5.2: Targeted maneuver

By releasing both the time needed to maneuver and the final true anomaly from any constraints, the optimization tool will try to bring the time up to a virtually infinite value in order to have infinitesimal thrust impulses only at the perigees, where the maneuver is most efficient. To highlight this phenomenon and the capabilities and limits of the tool the solutions that follow were found by cyclically fixing the maneuver time and then releasing it to find the next solution with a continuation approach. Therefore, the tool has been exploited with both modes from the right-hand-side of graph 5.2, but the same could be achieved by working with the two left-hand-side-modes in the same way.

5.2.1 Differential Correction - Jacobian Matrix

As mentioned in chapter 2 what drives a guess solution to the actual solution is a differential corrector that exploits Newton's method. The purpose of this section is to highlight how the Jacobian matrix was built for the two modes that were used in this example.

Free-time, free-anomaly
This is the case mentioned above, nine unknowns and nine boundary conditions define a 9×9 Jacobian matrix:

$$
\boldsymbol{G} = \begin{pmatrix}
\frac{(\delta x_f)_p - \delta x_f}{\Delta_{\lambda x}} & \frac{(\delta x_f)_p - \delta x_f}{\Delta_{\lambda y}} & \cdots & \frac{(\delta x_f)_p - \delta x_f}{\Delta_\nu} & \frac{(\delta x_f)_p - \delta x_f}{\Delta_t} \\
\vdots & \vdots & \ddots & \vdots & \\
\frac{(\delta \lambda_{mf})_p - \delta \lambda_{mf}}{\Delta_{\lambda x}} & \frac{(\delta \lambda_{mf})_p - \delta \lambda_{mf}}{\Delta_{\lambda y}} & \cdots & \frac{(\delta \lambda_{mf})_p - \delta \lambda_{mf}}{\Delta_\nu} & \frac{(\delta \lambda_{mf})_p - \delta \lambda_{mf}}{\Delta_t} \\
\frac{(\text{free}\nu)_p - \text{free}\nu}{\Delta_{\lambda x}} & \frac{(\text{free}\nu)_p - \text{free}\nu}{\Delta_{\lambda y}} & \cdots & \frac{(\text{free}\nu)_p - \text{free}\nu}{\Delta_\nu} & \frac{(\text{free}\nu)_p - \text{free}\nu}{\Delta_t} \\
\frac{(H_f)_p - H_f}{\Delta_{\lambda x}} & \frac{(H_f)_p - H_f}{\Delta_{\lambda y}} & \cdots & \frac{(H_f)_p - H_f}{\Delta_\nu} & \frac{(H_f)_p - H_f}{\Delta_t}
\end{pmatrix} \tag{5.21}
$$

where δ stands for the mismatch between the obtained and the desired value, the subscript p means perturbed and freeν is the condition expressed in equation (5.16).

The Jacobian matrix is calculated iteratively by column, by perturbing each guess solution (the seven costates, the true anomaly and the time of maneuver) of a Δ, which is usually the same for every variable.

Notice that when perturbing the final true anomaly no integration of the system's ODEs is required since no initial value is perturbed in the IVP. This was

the reason why it was opted to perform Point-to-Orbit maneuvers and not viceversa.

Fixed-time, free-anomaly

When a specific time to maneuver is defined the unknowns become eight and there's no need to compute the Hamiltonian anymore, therefore the Jacobian matrix loses the last column and the last line to become an 8×8 matrix:

$$\boldsymbol{G} = \begin{pmatrix} \frac{(\delta x_f)_p - \delta x_f}{\Delta_{\lambda x}} & \frac{(\delta x_f)_p - \delta x_f}{\Delta_{\lambda y}} & \cdots & \frac{(\delta x_f)_p - \delta x_f}{\Delta_\nu} \\ \vdots & \vdots & \ddots & \vdots \\ \frac{(\delta \lambda_{mf})_p - \delta \lambda_{mf}}{\Delta_{\lambda x}} & \frac{(\delta \lambda_{mf})_p - \delta \lambda_{mf}}{\Delta_{\lambda y}} & \cdots & \frac{(\delta \lambda_{mf})_p - \delta \lambda_{mf}}{\Delta_\nu} \\ \frac{(\text{free}\nu)_p - \text{free}\nu}{\Delta_{\lambda x}} & \frac{(\text{free}\nu)_p - \text{free}\nu}{\Delta_{\lambda y}} & \cdots & \frac{(\text{free}\nu)_p - \text{free}\nu}{\Delta_\nu} \end{pmatrix} \tag{5.22}$$

5.2.2 Results

The two proposed results presented in this section demonstrate the distinctions between a low maneuver time solution and a high one. Subsequently, a parametric analysis of the initial costates is provided.

Low maneuver time solutions

In these types of solutions, propulsion is active for the majority of the time. As illustrated by the switching function 5.5 and the two-dimensional and three-dimensional representations of the trajectory 5.6, brief coasting arcs remain present and cannot be eliminated. Convergence difficulties occur with lower maneuver times, as these coasting phases allow for the thrust angles to invert their trend without causing disturbance in the solution determined by the relatively high thrust. It is important to note that these are not minimum time solutions, as those would require a different set of terminal conditions.
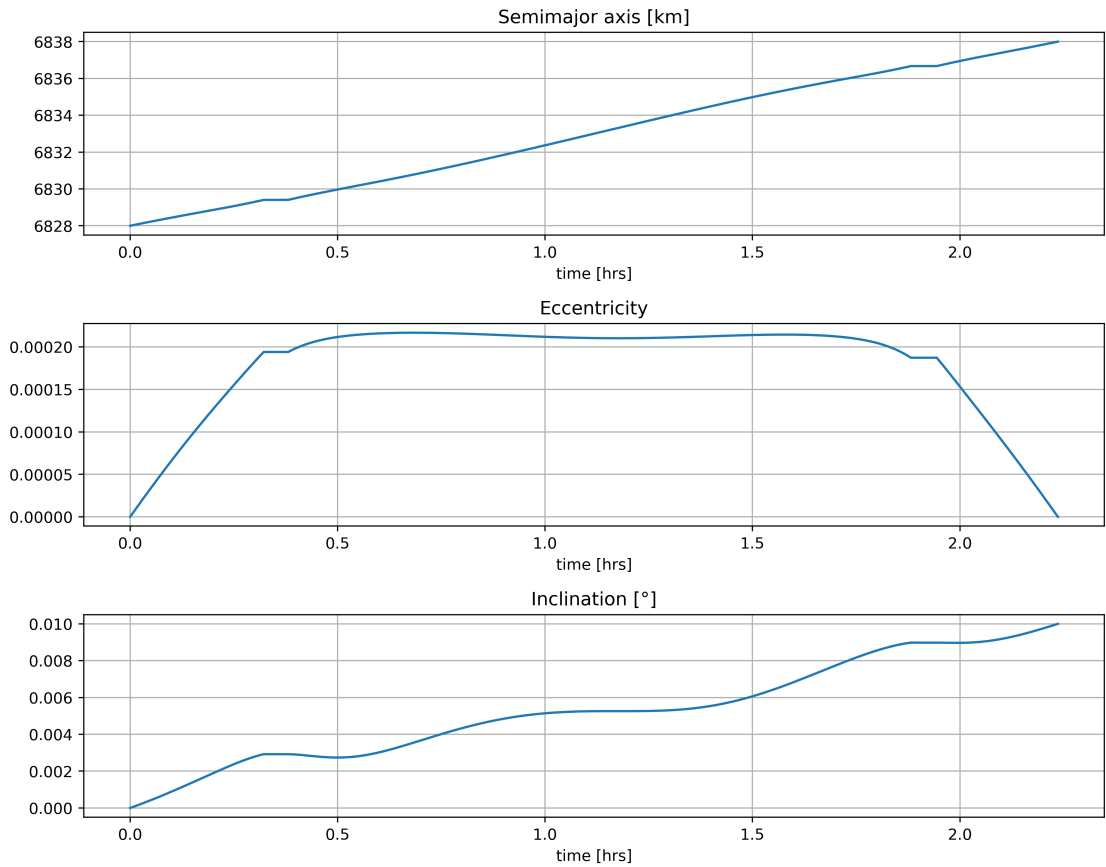
Figure 5.3: Semimajor axis, eccentricity and inclination during the maneuver

As it can be seen from the evolution of the first three keplerian parameters, the orbit is raised and inclination is changed almost continuously, as expected. The tool is able to bring the eccentricity of the final orbit back to the targeted value (0) by defining a last propulsive burst.
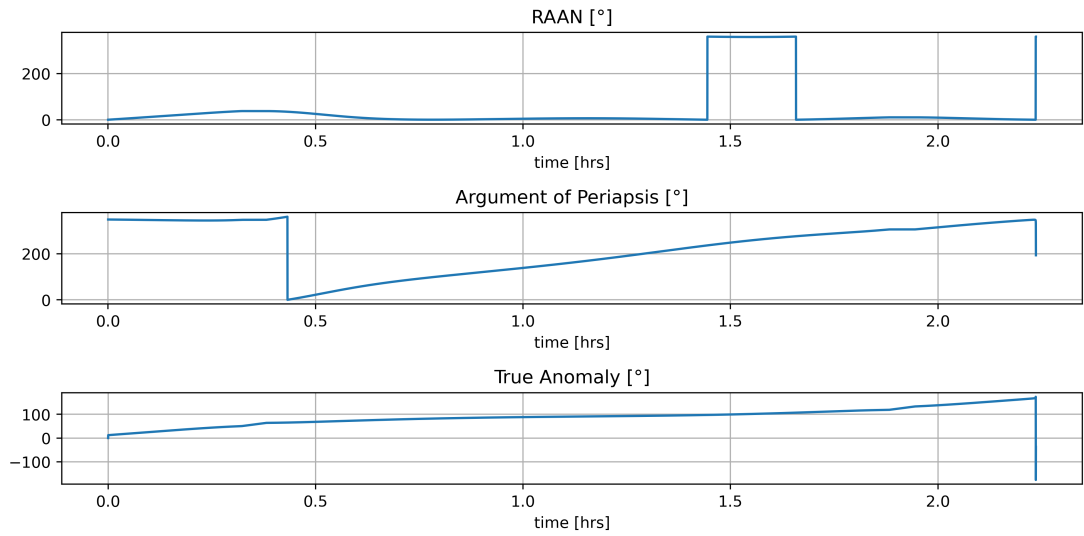
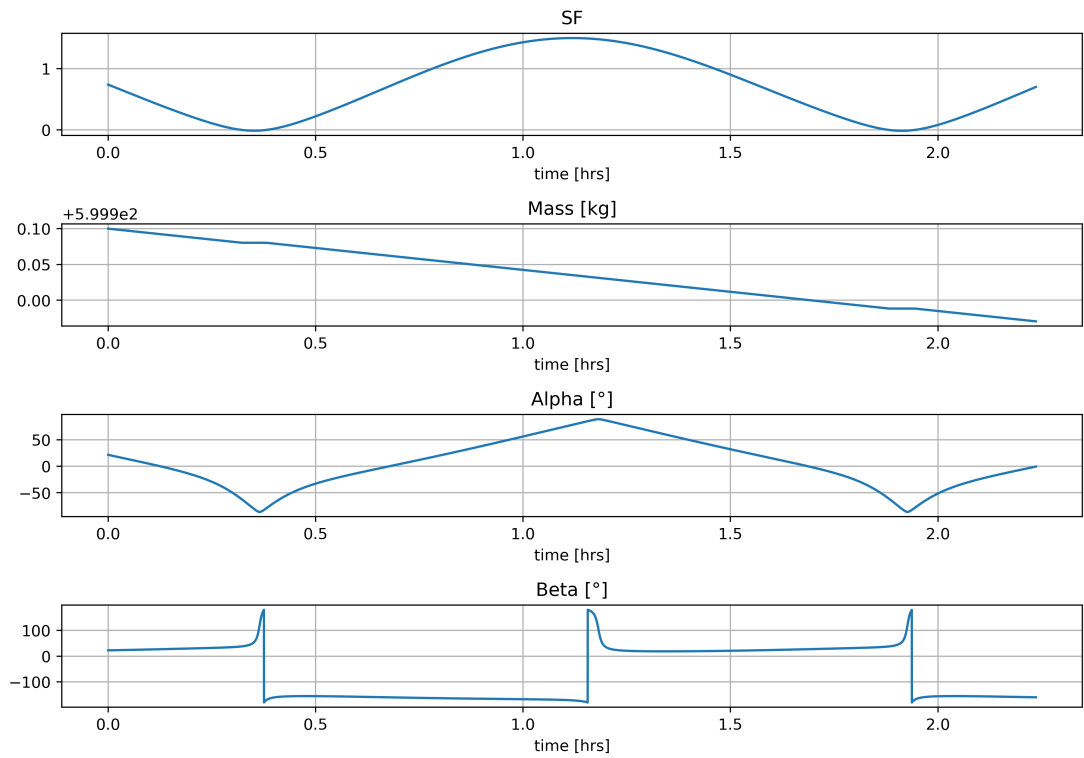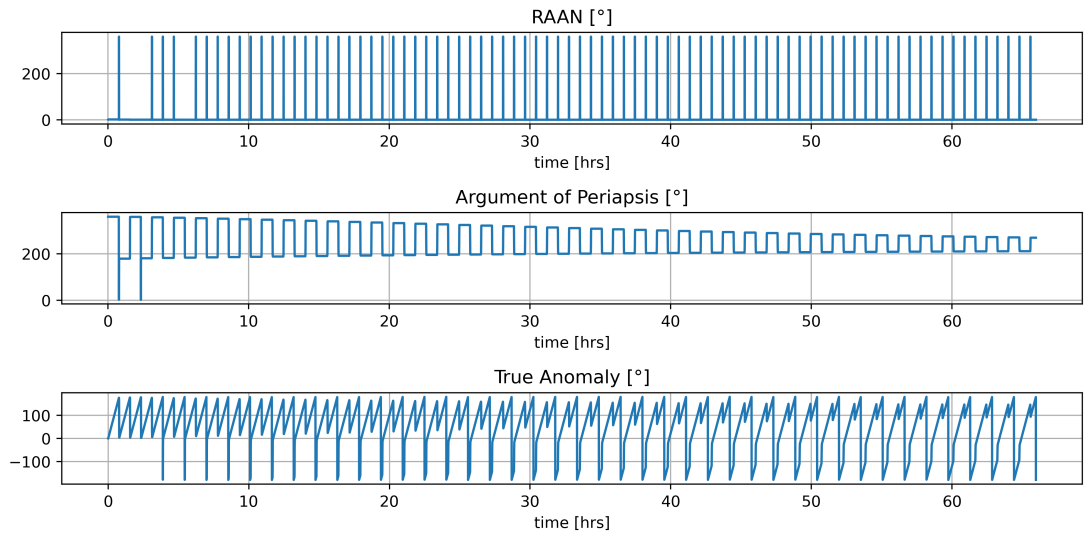**Figure 5.4:** RAAN, argument of periapsis and true anomaly during the maneuver

**Figure 5.5:** switching function, mass and thrust angles during the maneuver

53

The in-plane thrust angle α testifies that thrust is not provided along the velocity vector, therefore allowing for shorter maneuver times, at the expenses of efficiency. The out-of-plane thrust angle β switches from positive to negative values depending on where the spacecraft is along the orbit: utilizing the out-of-plane angle φ from the J2000 polar coordinate system, when the spacecraft travels from φ_{min} to φ_{max} the β angle is positive, whereas when the spacecraft travels in the remaining portion of the orbit the β angle is negative.

(a) Trajectory in initial perifocal plane   **(b)** Trajectory in J2000 RF
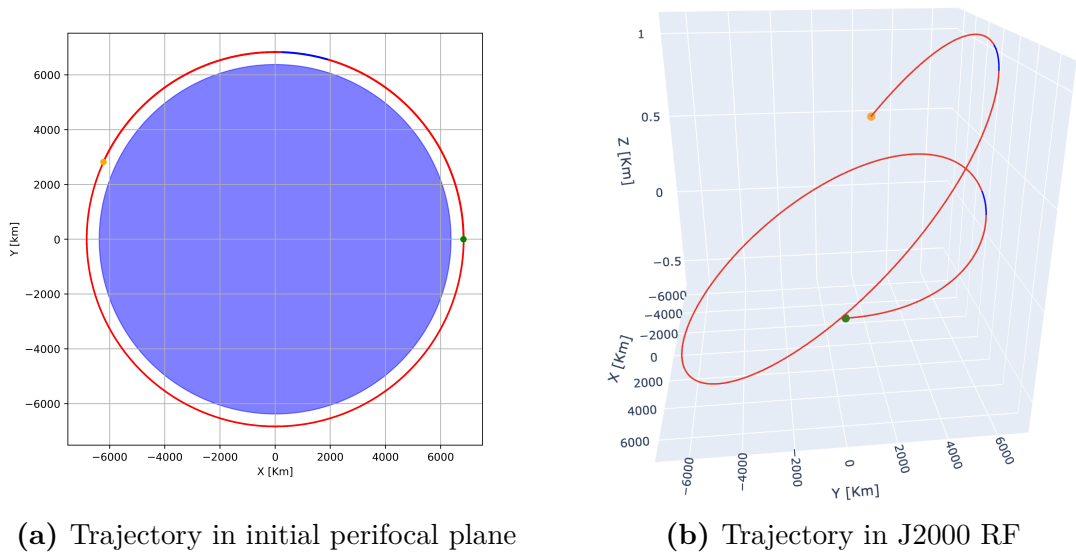
Figure 5.6: Low maneuver time trajectory

High maneuver time solutions

This was the highest maneuver time that allowed for convergence. It is noticeable from the switching function graph that the thrust-coast structure of this solution is fairly complicated and pushes the boundaries of what can be achieved without defining an a-priori arc structure: minimal changes in the initial conditions can cause great variations to the final condition and solution divergence is highly probable if the K1 and K2 relaxation parameters are not set correctly.
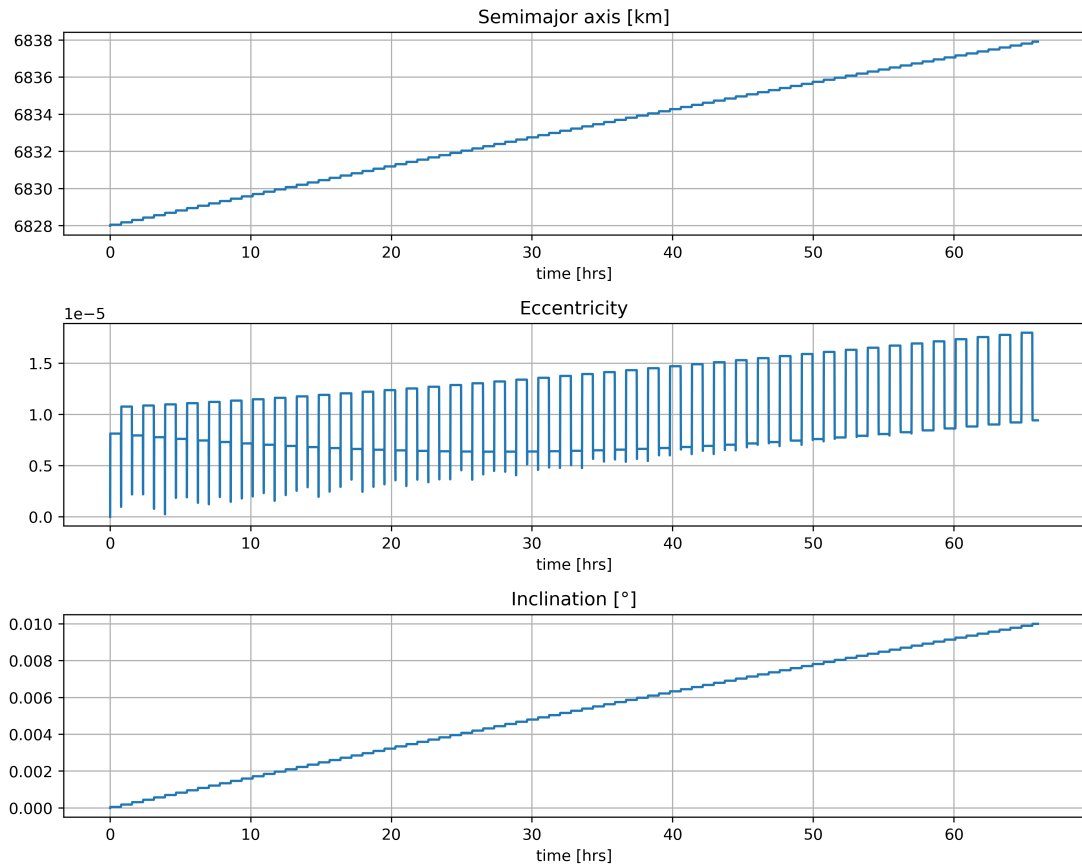
Figure 5.7: Semimajor axis, eccentricity and inclination during the maneuver

With a comparable precision to the low-maneuver-time case, the semimajor and inclination targeted values are reached. The optimization tool wasn't able to fully satisfy the eccentricity constraint, however, its low value allows the solution to be considered valid. As mentioned, the high times involved in this IVP cause the convergence to be fairly complicated, and parameters that are not directly targeted, such as the eccentricity (which is rendered through the velocities in the terminal conditions), can be hard to obtain precisely.

Figure 5.8: RAAN, argument of periapsis and true anomaly during the maneuver
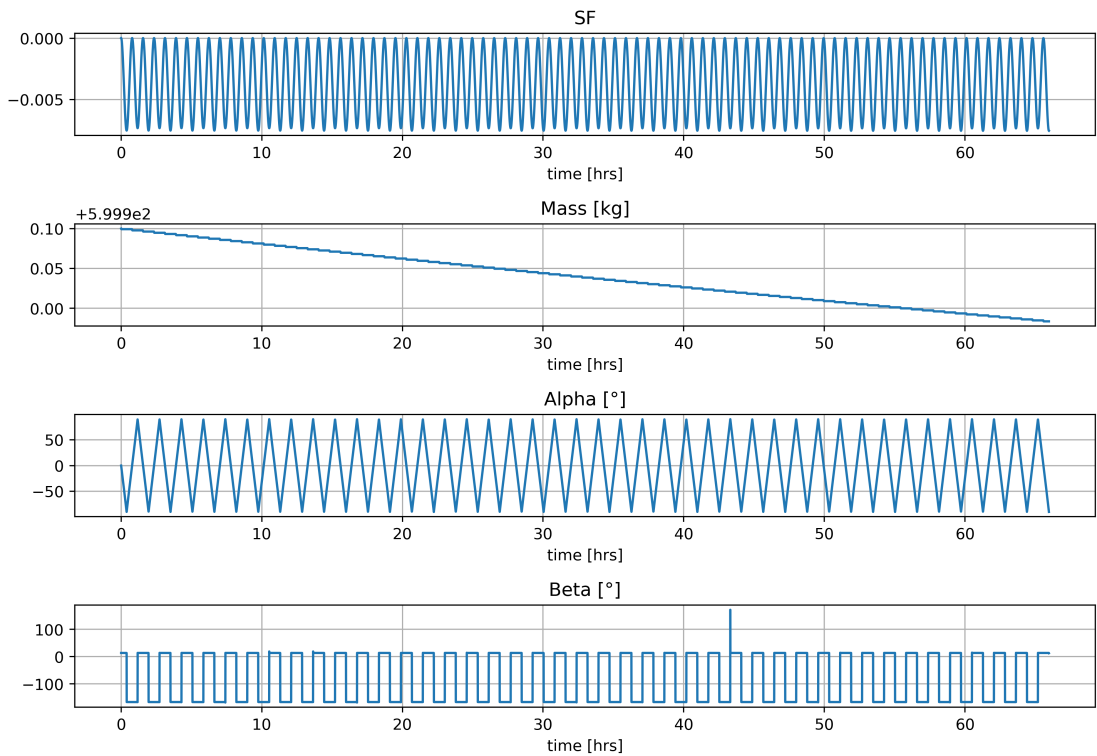
Figure 5.9: switching function, mass and thrust angles during the maneuver

(a) Trajectory in initial perifocal plane

(b) Trajectory in J2000 RF
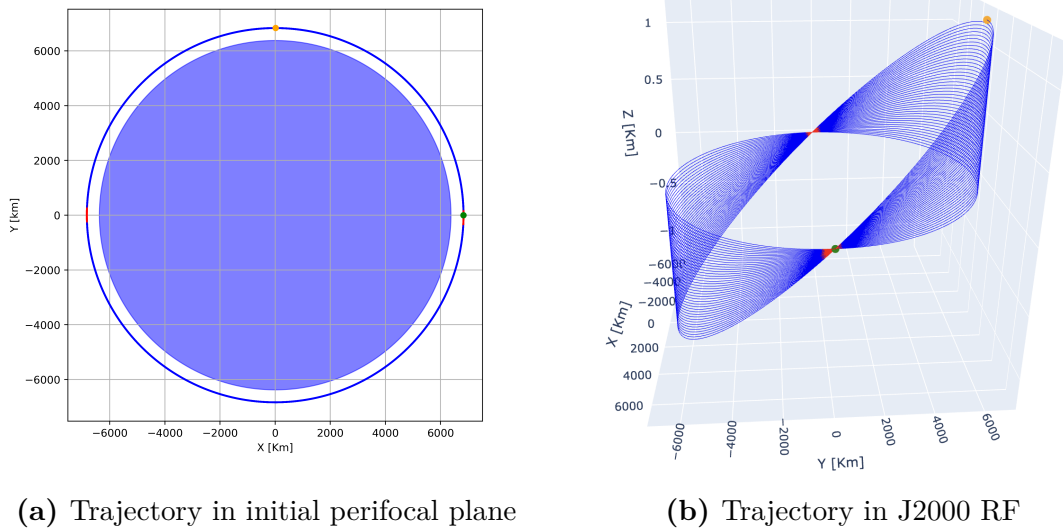
Figure 5.10: High maneuver time trajectory

The in-plane thrust angle α testifies that, when provided, thrust acts mostly along the velocity vector ($\alpha = 0$), which is the most propellant efficient orbit raising strategy. The out-of-plane thrust angle β determines the inclination change by not being exactly zero or -180.

The first solution presented is similar to what can be expected from using Edelbaum's approximation of continuous low-thrust orbital transfer maneuvers, although the simplifying hypotheses of that approach are not fully met here: the transfer orbit should be nearly circular and the orbital plane variation should be minimal. On the other hand, the high-time maneuver solution shows a more efficient maneuver where thrust is provided only at the nodes. The thrust direction is defined to combine (with a vectorial sum) the Delta V needed to change the energy of the orbit (and cause its rise) with the Delta V required to achieve the target orbital plane.

When the thrust misalignment is small, as in the latter solution, the orbital plane change has little influence on the total Delta V required. With more time to maneuver, the thrust misalignment for each infividual burn can be reduced, hence reducing the total Delta V required; confirmation of the trend can be found in graph 5.11.

Parametric analysis

As stated above, the optimization tool was exploited, for this example, to find solutions with progressively higher maneuver times. The solutions' trend can be easily seen in this graph:
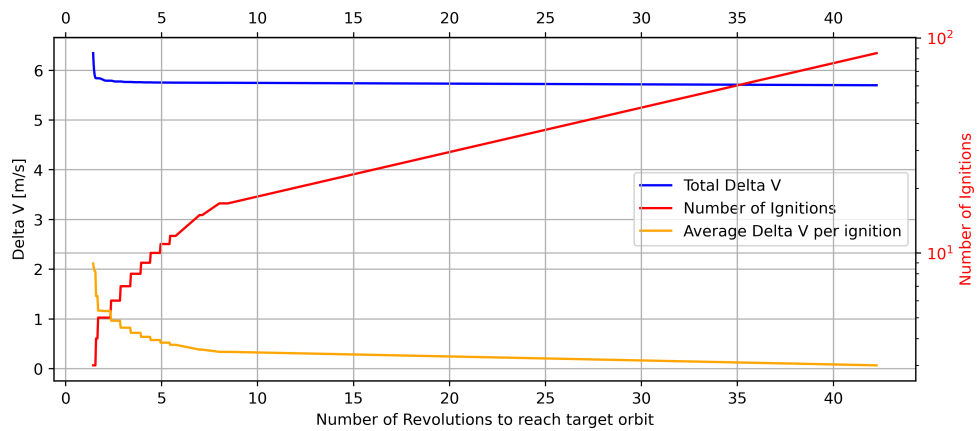

Figure 5.11: Solution behaviour against number of revolutions

As evidenced by the number of ignitions curve, consistent data from converged solutions was successfully retrieved until approximately six orbital periods of maneuver time. Subsequently, only a few convergences were obtained. Although partially explained in the previous section, the reason for this convergence difficulty is most evident by looking at the following graphs, where the initial costates were plotted for every converged solution:
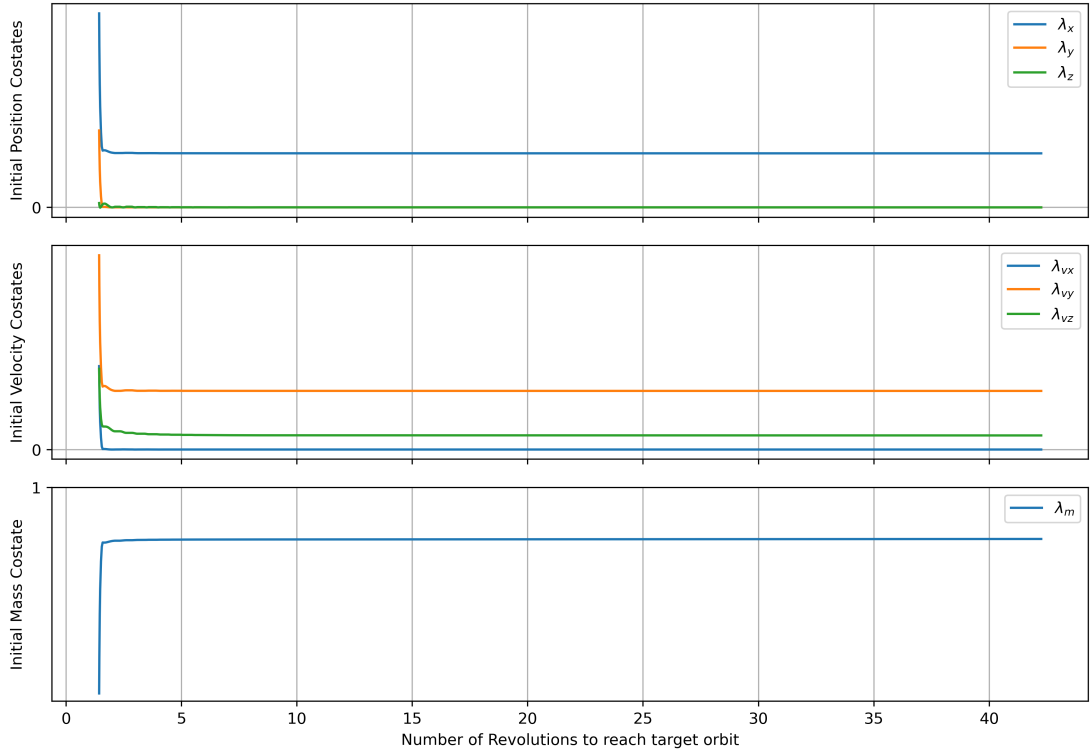
Figure 5.12: Parametric analysis of initial costates

Strong gradients in the initial costates suggest that fairly considerable changes in the initial guesses don't cause solution divergence, in this case the differential corrector can be set to work in the best conditions and provides convergence in a few seconds if a good initial guess is provided. On the contrary, when the initial costates have a nearly null gradient the smallest initial delta can cause serious solution oscillation. With this scale it is almost impossible to discern a difference between a 10 orbital periods solution from a 40 orbital periods one, which denounces bad conditioning for the differential corrector to work properly. For these reasons, when the thrust-coast structure becomes too complicated, an a-priori arc structure definition is advised, along with a multiple shooting approach.

It is also worthy of note that the strongest position costate is the one linked to the x value, since the satellite's initial position is on the x axis. On the contrary, the strongest velocity costate is the one linked to v_y which represents the initial along-track velocity and is the most important value when considering a delta semimajor-axis-maneuver.

Chapter 6

Collision Avoidance Trajectories

As explained in the previous chapter, the preferred maneuvering strategy in this research is a semimajor axis variation. Because the optimization tool lacks the perturbative accelerations that characterize a LEO environment, an important precaution was adopted in this work: the primary spacecraft orbits Earth with a circular trajectory and, if needing to perform a CAM, it has to target an also circular evasion orbit. This is done to eliminate potential inaccuracies in the PoC calculation resulting from apsis rotation of elliptical orbits, which is a perturbative effect that arises due to Earth's asphericity.

In order to simulate an actual scenario, the primary spacecraft's propulsion characteristics were based on a datasheet from state-of-the-art Hall-effect thrusters suitable for use as main propulsors in small-sized satellites. The case study is set in the lower region of the LEO environment, which is the typical operational domain for these kinds of spacecraft.

6.1 Case study

Two objects of interest were modeled in the PoC tool with the following keplerian elements:

Name	a [km]	e [deg]	i [deg]	Ω [deg]	ω [deg]	ν [deg]
Primary	$R_e + 300.000$	0.00	45.00	1.00	0.00	1.00
Secondary	$R_e + 300.155$	0.00	-0.01	0.00	0.00	0.99

Table 6.1: Example satellites' keplerian parameters

For the purposes of this illustrative example, both satellites have initial circular orbits and the same geometric and mass properties:

$$r_{sat-p} = r_{sat-s} = 1\text{m} \tag{6.1a}$$

$$m_{sat-p} = m_{sat-s} = 150\text{kg} \tag{6.1b}$$

The primary spacecraft has a Hall-effect thruster with the following specifications:

$$I_{sp} = 1400\text{s} \qquad T = 0.025\text{N} \tag{6.2}$$

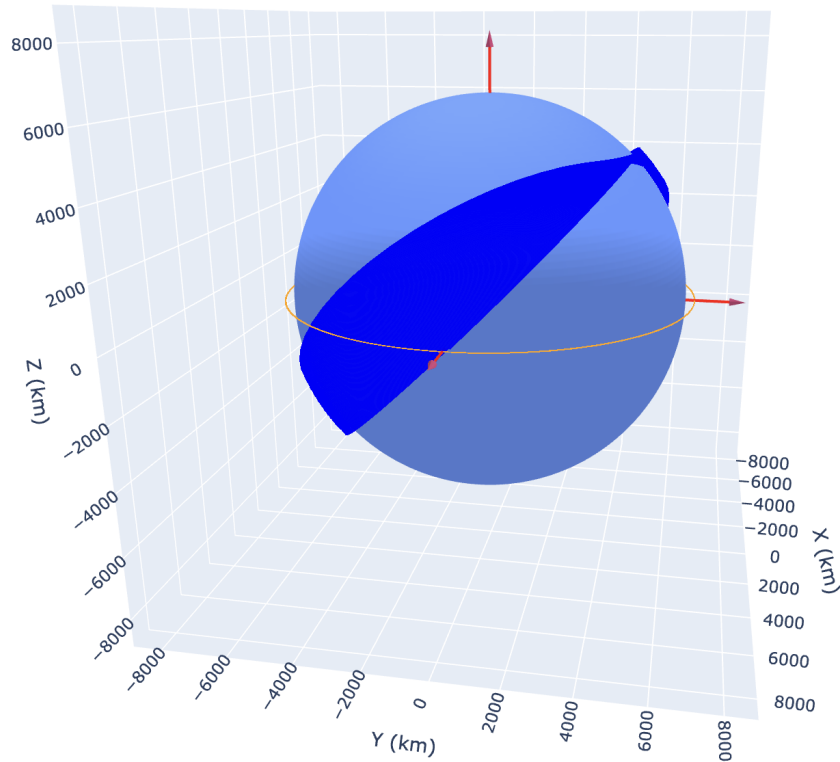By propagating both satellites in the high-fidelity LEO model the following trajectories are found:

Figure 6.1: Propagated example orbits: blue = primary s/c, orange = secondary s/c

A potential collision is found after approximately 2 orbits of propagation:

61

TCA [s]	d_{close} [km]	PoC
10818.04	0.107284	3.614×10^{-4}

Table 6.2: Conjunction event

According to the safety standards defined in section 4.3, a collision avoidance maneuver is hereby required. By following the algorithm represented in 4.3, the least propellant demanding maneuver that lowers the probability of collision below 1×10^{-4}, is found to be a semimajor axis lowering of 19 meters, rounded up to the nearest integer. The evasion maneuver yelds the following results:

TCA [s]	d_{close} [km]	PoC	Δa [km]	m_p [kg]	t_{CAM} [s]
10818.53	0.388371	9.959×10^{-5}	-0.019	1.192×10^{-5}	667.76

Table 6.3: Conjunction event after the CAM and CAM data

The following figure summarises the variation of the primary spacecraft's keplerian elements during the evasion maneuver along with the switching function and optimal thrust angles.

62
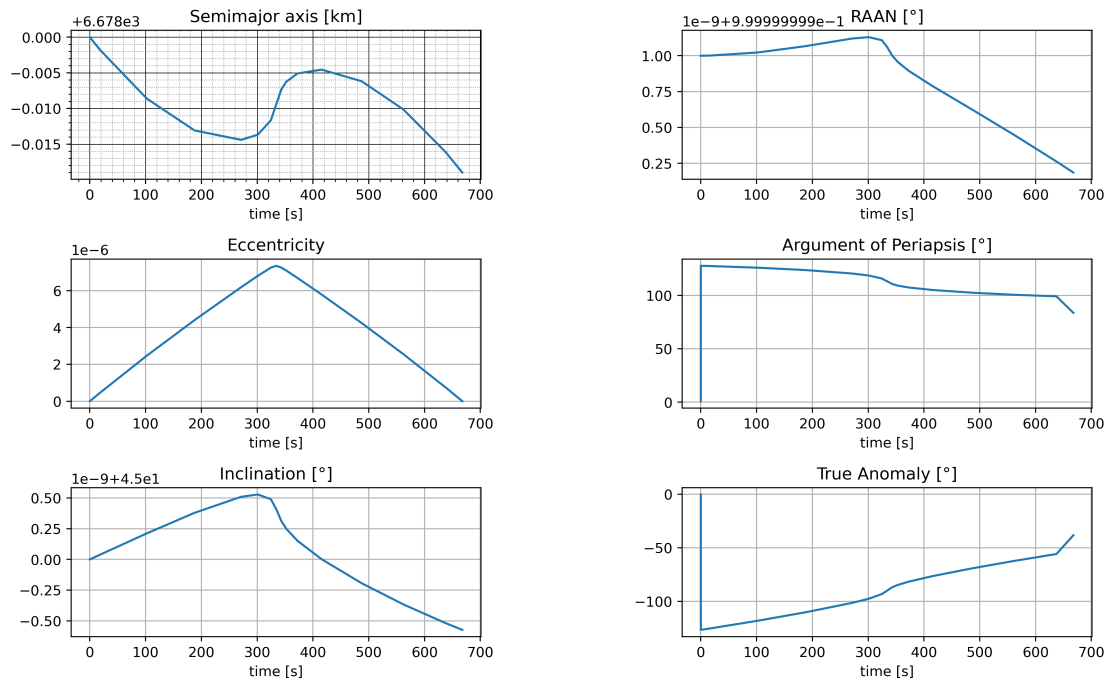
(a) Semimajor axis, eccentricity and inclination during the maneuver

(b) RAAN, argument of periapsis and true anomaly during the maneuver
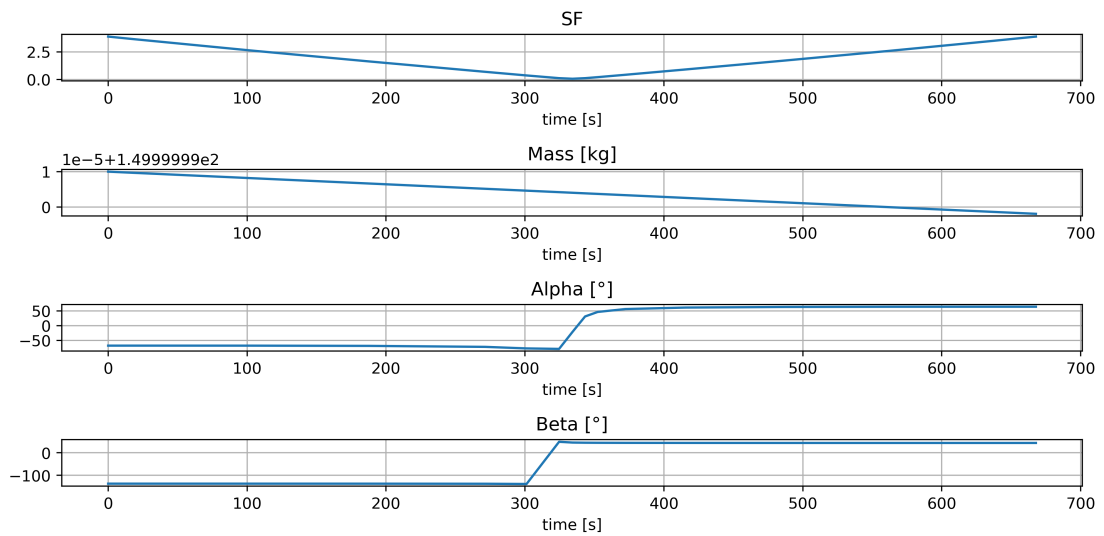
(c) Switching function, mass and thrust angles during the maneuver

Figure 6.2: Evolution of spacecraft and control variables during the selected CAM

The semimajor axis behavior during the identified maneuver can be misleading:

63

by not being monotonically decreasing, it may induce the wrongful idea of the maneuver not being optimal for its case. As the J2000 polar coordinates in the next figure clarify, the radius is in fact monotonically decreasing, while the semimajor axis isn't. This is a consequence of the eccentricity requirement, which dictates the circularization of the targeted orbits and therefore causes semimajor axis variation.

(a) J2000 polar coordinates   (b) ZEN velocities
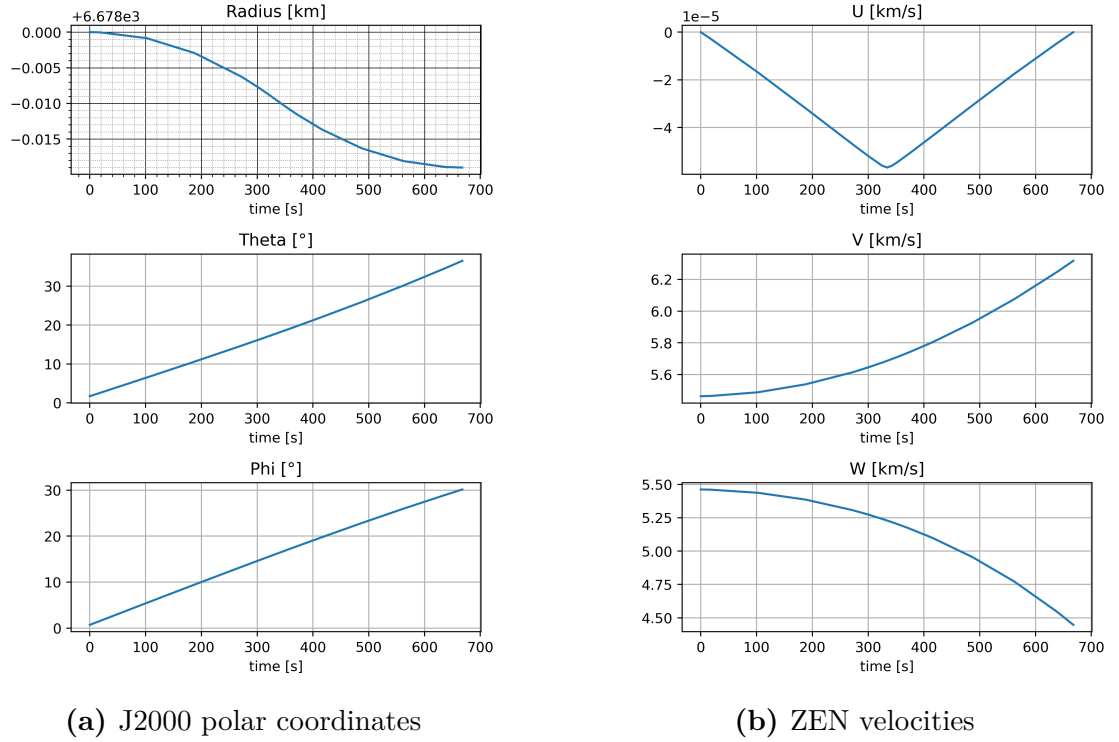
Figure 6.3: Evolution of spacecraft's state in J2000/ZEN coordinates during the selected CAM

Note that the radial component of the velocity starts and ends at zero, confirming that the initial and final orbits are in fact circular, and the east and north components evolve along the trajectory according to the orbital plane's inclination: the closer to the ascending node ($\varphi = 0$), the higher the north component w is, and, the closer is the out-of-plane angle φ to the orbit's inclination, the higher the east velocity component v.

6.1.1 Parametric Analysis of results

In order to extrapolate additional useful insights from this example a parametric evaluation of the maneuver to be performed by the primary satellite was carried out with the trajectory optimization tool. Iteratively the tool evaluated a Hohmann-like maneuver with a target delta semimajor axis spanning between -50m and $+50$m. A constant $\Delta a = 10$m step was adopted to find the first solutions, using a continuity approach, additional solutions where found by setting $\Delta a = 5$ between the solutions that yielded the best results in terms of PoC. The following graphs highlight the evolutions of the solutions' keplerian parameters, polar J2000 positions and ZEN velocities as well as the controls and the spacecraft's mass:
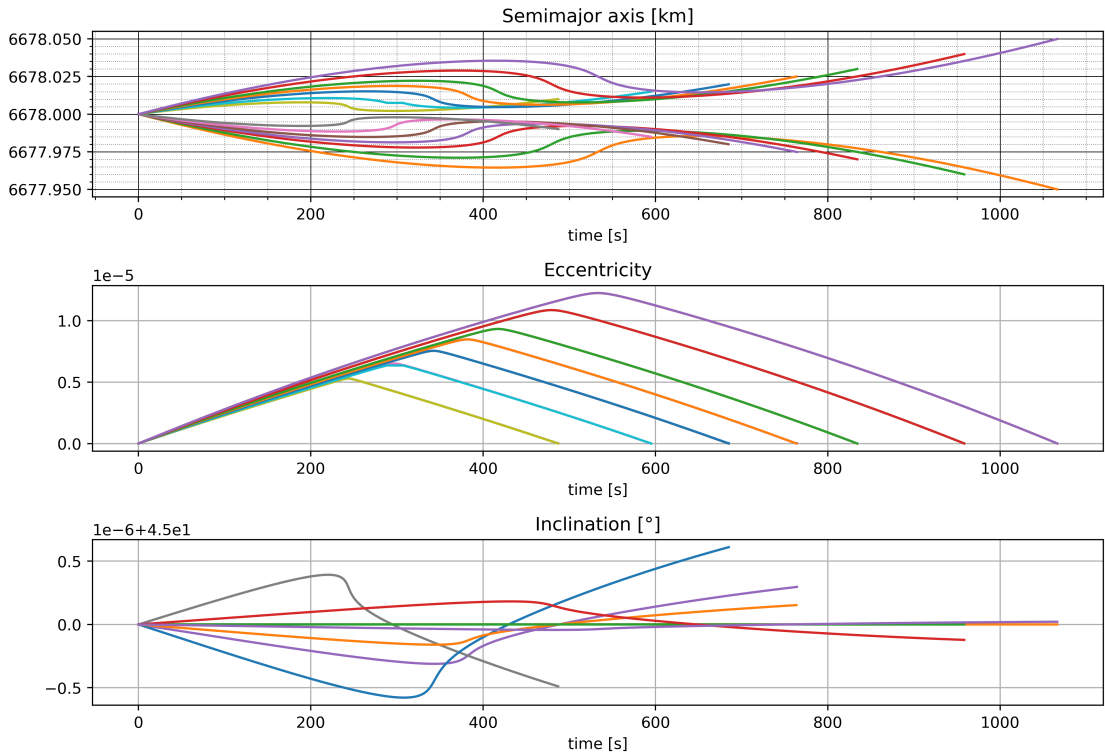
Figure 6.4: Semimajor axis, eccentricity and inclination during the evaluated maneuvers

The same considerations made for figure 6.2 about the semimajor axis variation apply here. The J2000 polar coordinates provided later on should clarify the trends.
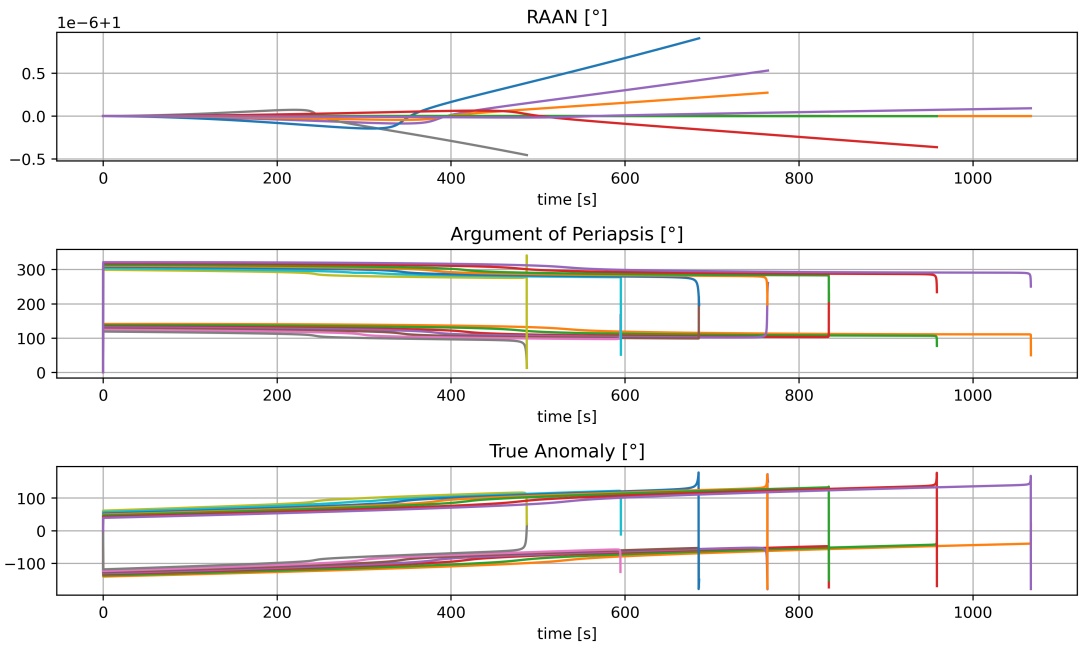
65

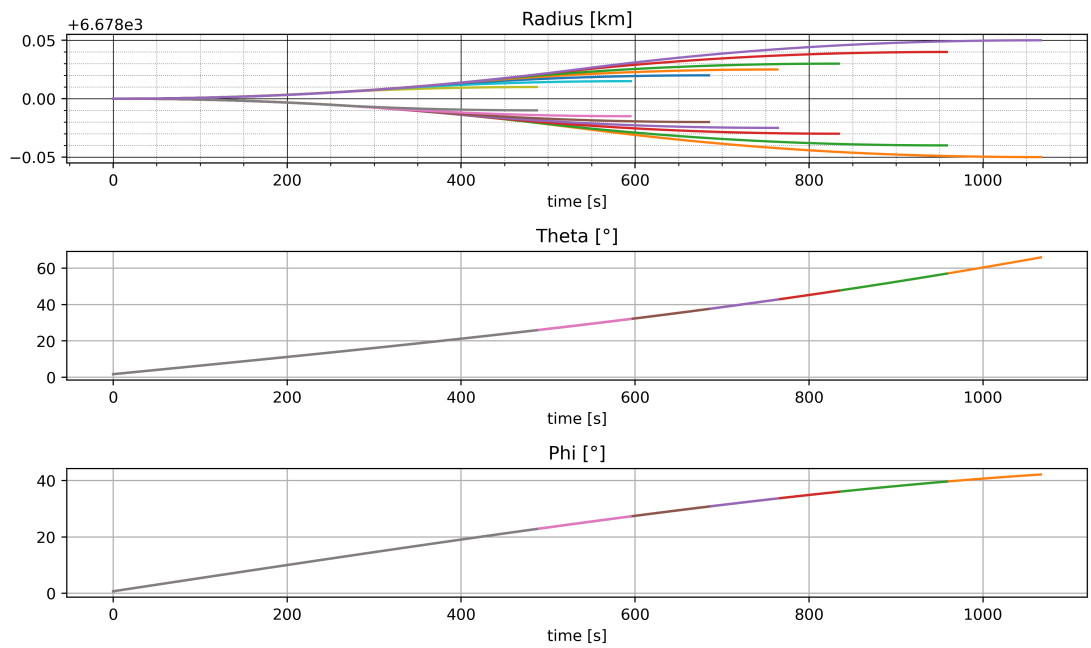**Figure 6.5:** RAAN, argument of periapsis and true anomaly during the evaluated maneuvers

Figure 6.6: J2000 Polar coordinates during the evaluated maneuvers

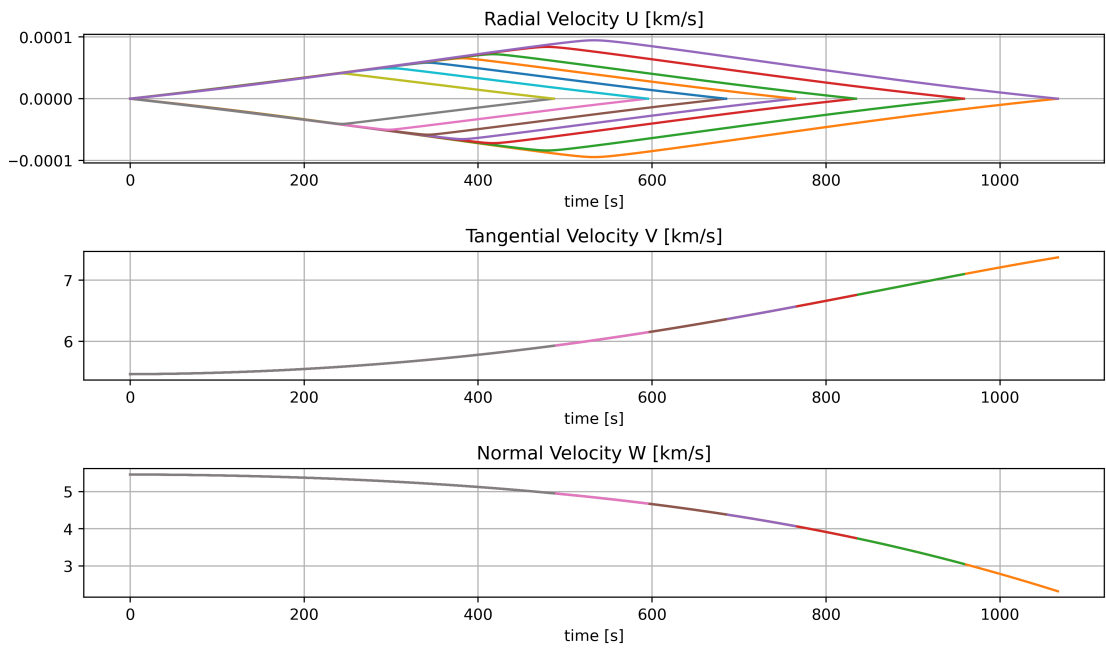**Figure 6.7:** ZEN velocities during the evaluated maneuvers
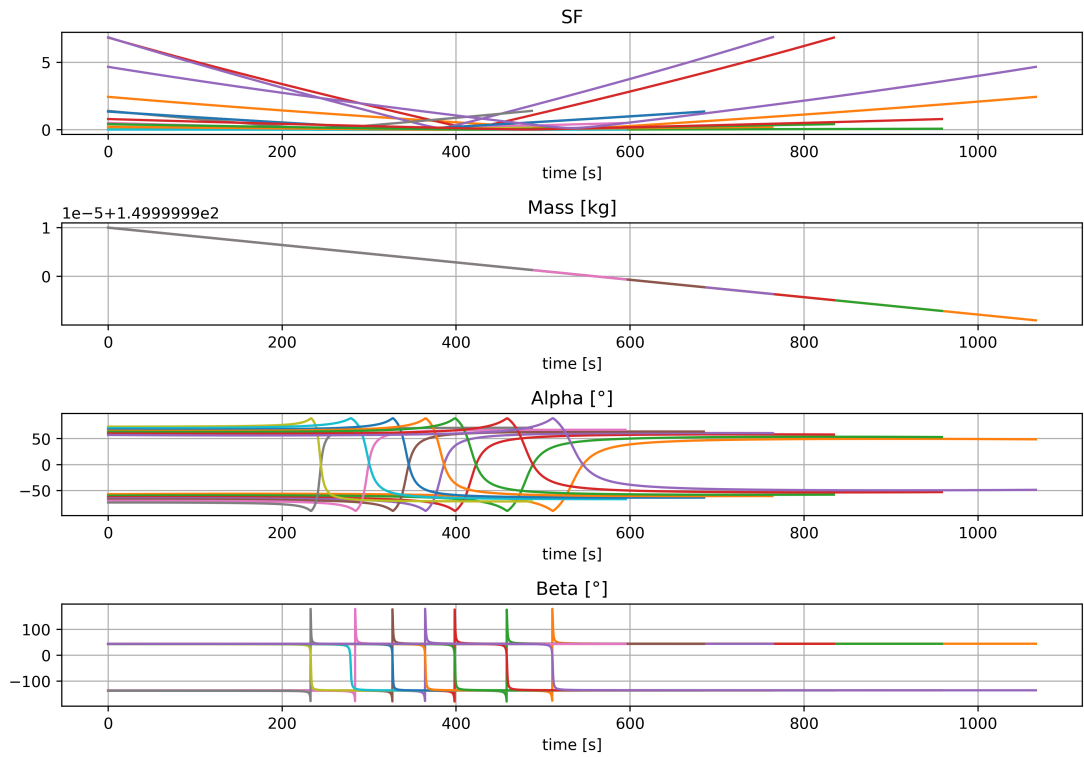
Figure 6.8: switching function, mass and thrust angles during the evaluated maneuvers
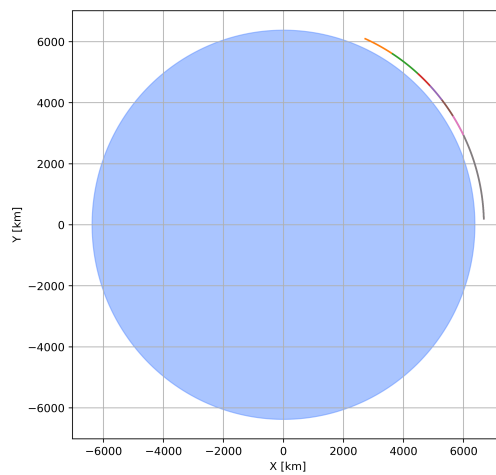

Figure 6.9: 2D trajectories in the orbital plane

68

As illustrated in the switching function graph 6.8, all solutions identified are characterized by the presence of continuous propulsion. The sole exception is the case of $\Delta a = +15$m, which exhibited a brief coasting phase (visible in the semimajor axis graph 6.4, light blue line). The reasons for this behavior can be attributed to the extremely small state variations targeted, paired with a low-thrust control and, possibly, the lack of an a-priori arc definition. Furthermore, the time of maneuver was set to be free, but bounded to a maximum value of an orbital period, which precludes the possibility for the solution to have multiple thrusting arcs at perigees, where theoretically most efficient. This was an author's decision related to this trajectory optimization's objectives of providing short-term evasion maneuvers, and that certainly helped in obtaining convergence by reducing the solutions search space. Moreover, with the selected propulsive parameters, the problem's objective of maximizing the final mass is mostly affected by the thrust time, rather than by the kind of trajectory, hence the optimizer is more prone to reducing the overall maneuver time. All of the identified solutions exhibit a similar structure: when the objective is to raise the orbit, a first phase in which the thrust vector is oriented along the direction of the velocity, with a radial component, is followed by a second circularizing phase in which thrust is provided against the velocity, viceversa happens in the case of an orbit lowering.

The following graphs highlight the fundamental simmetry between the identified orbit raising and orbit lowering solutions:
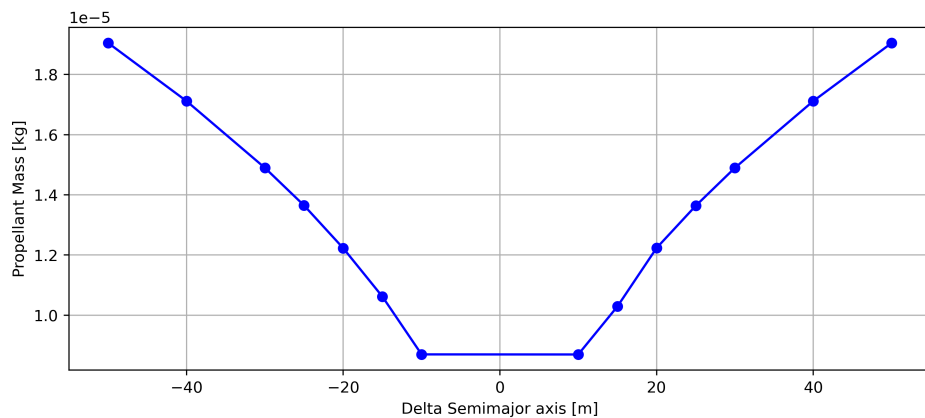

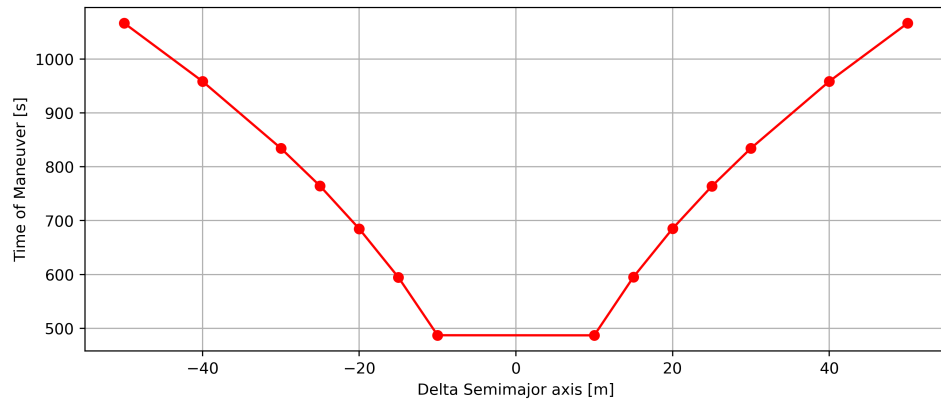**Figure 6.10:** Trajectory in initial perifocal plane

Figure 6.11: Trajectory in J2000 RF

In light of these results, it can be reasonably concluded that the repositioning maneuver to be performed following TCA should bear a strong resemblance to the CAM in terms of propellant expenditure and time to maneuver.

Risk Evaluation

The curve below relates the considered maneuvers to their corresponding PoC computation and highlights the better fitness of negative semimajor axis variation solutions, as expected, since they ensure greater radial separation between the primary and the secondary spacecrafts.
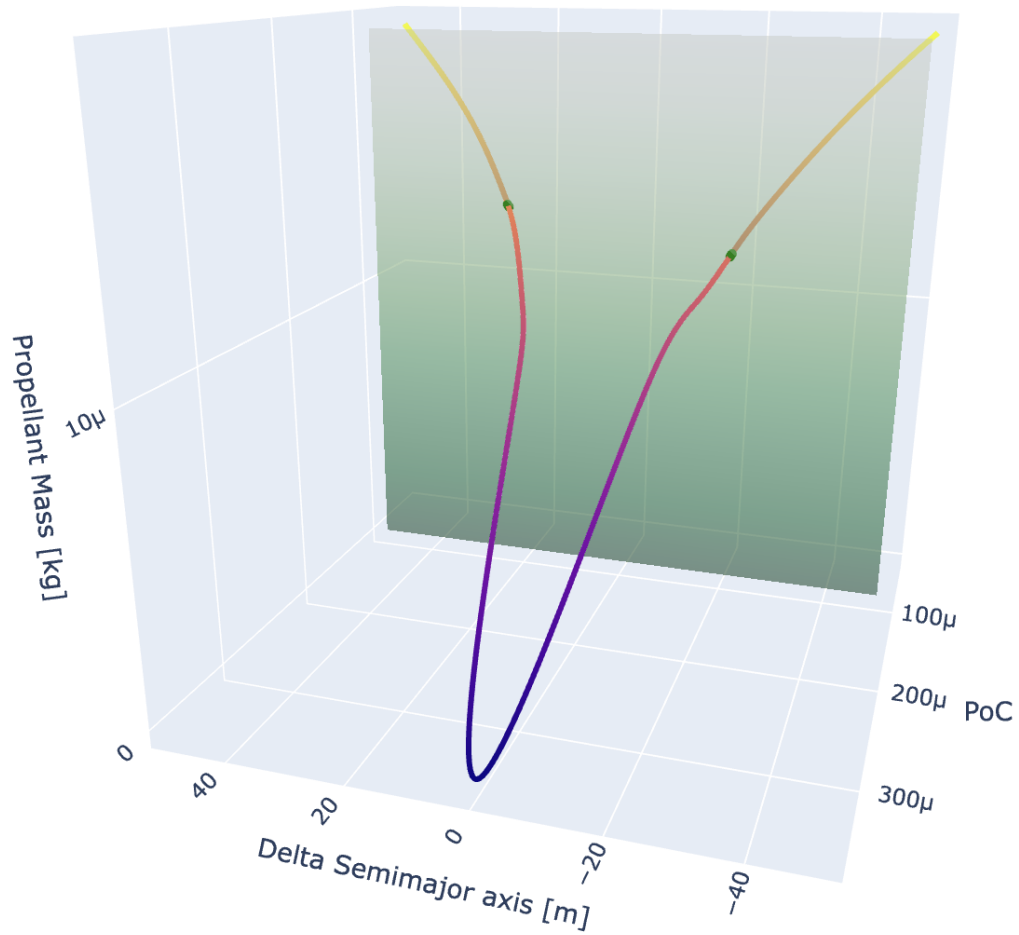

Figure 6.12: PoC evaluation for each candidate maneuver

Initial Costates

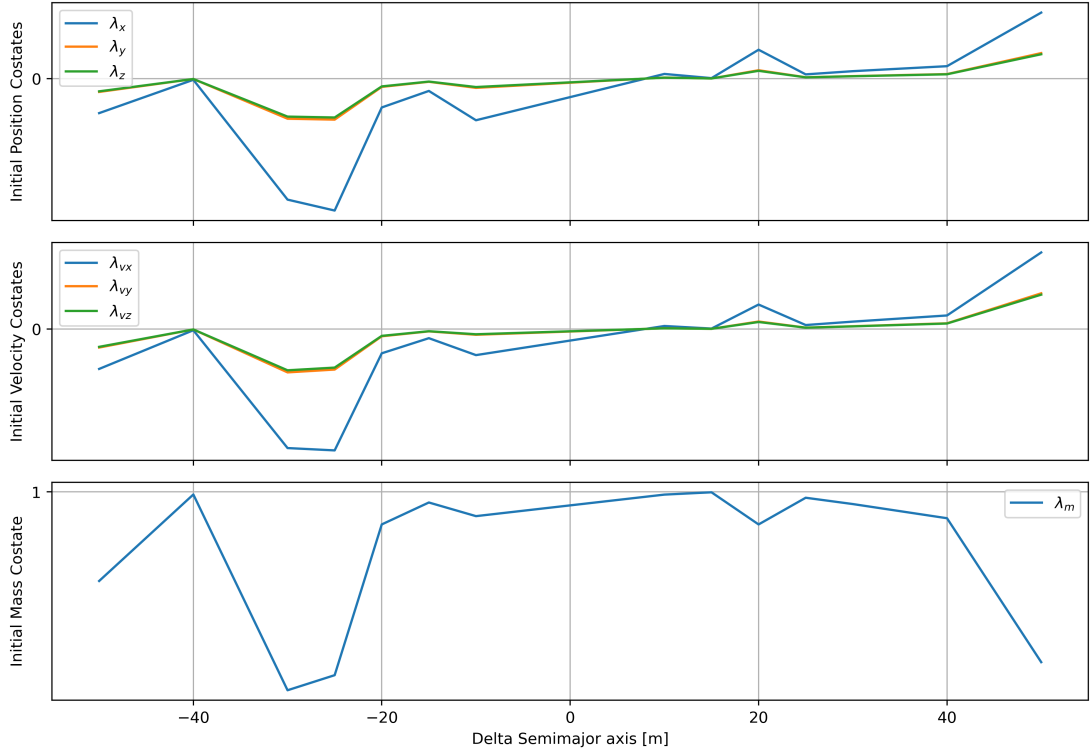By plotting each solution's initial costates other observations can be made:

Figure 6.13: Initial costates for each solution

Although lacking a physical significance and a clear predictable trend, initial costates can provide valuable insights into a solution's behavior. With experience and critical analysis of the results, sensible guesses can be made. By recognizing that a typical Hohmann-like maneuver has a thrust-coast-thrust structure (TCT), it can be deduced that the initial switching function should be positive. A relationship between the primer vector and the mass costate is established by the definition of the SF 5.8b and is evident in the graph above: when the primer vector rises in module, the mass costate plummets, and vice versa. From the definition of the thrust angles in terms of velocity costates 5.7, it is possible to predict the former if the direction of the initial thrust is known: as mentioned above, the identified trajectories have predictable along-track, along-velocity or against-velocity initial thrust and the graph above confirms the trend in terms of positive or negative initial velocity costates. Although with a different scale, which is here omitted since it is determined by the problem's optional adimensionalization, the initial position costates follow an almost identical trend compared to the velocity ones.

It is important to notice how the dominant costate is related to the x-coordinate, as the primary spacecraft's initial position in the J2000 RF is almost coincident with the x axis. Different co-dependencies can be expected with different initial positions.

Parametric analyses of converged solutions are of great importance for the comprehension of costate behaviour, and can be of significant assistance with initial guesses, which, under the influence of the specific characteristics of the optimization problem, can considerably impact the convergence capabilities of the presented method.

73

Chapter 7

Closing Remarks and Future Development

The work's objective of developing a fully functional optimization tool based on the indirect transcription of the optimal control problem was widely met. Moreover, this work allowed for the modeling of a typical LEO environment, along with a basic methodology for the development of a conjunction analysis tool. By providing practical examples that cover the entire process followed to develop the optimization tool, the author hopes to contribute to a further understanding of the method and its applicability.

Evasion maneuvers push the boundaries of what can be achieved with indirect methods: the high precision required and the extremely low variation between initial and target states cause convergence to be difficult and obtainable only when initial guesses are good; critical analysis of the results and of the optimal costates was provided to help in this direction.

By following a homotopy-continuation approach, future developments of the optimization tool should gradually introduce LEO perturbations, and therefore allow for a complete coupling with the PoC computation tool. Furthermore, the translation from a TPBVP to a MPBVP with an inequality interior point constraint would guarantee a complete optimization of both the evasion and the re-positioning legs of the CAM, albeit greater problem complexity and convergence difficulties are to be expected.

Bibliography

[1] D.F. Lawden. *Optimal Trajectories for Space Navigation*. London: Butterworths, 1963 (cit. on p. 1).

[2] Burton G. Cour-Palais Donald J. Kessler. «Collision Frequency of Artificial Satellites: The Creation of a Debris Belt». In: *Journal of geophysical research* 83 (June 1978). URL: `https : / / web . archive . org / web / 20110515132446 / http : / / webpages . charter . net / dkessler / files / Collision%20Frequency.pdf` (cit. on p. 2).

[3] Luigi Mascolo. «Low-Thrust Optimal Escape Trajectories from Lagrangian Points and Quasi-Periodic Orbits in a High-Fidelity Model». PhD thesis. Torino: Politecnico di Torino, 2023. URL: `https://iris.polito.it/handle/ 11583/2976595` (cit. on pp. 4, 11).

[4] Manuel Soler David Morante Manueal S. Rivo. «A Survey on Low-Thrust Trajectory Optimization Approaches». In: (Mar. 2021). DOI: `10 . 3390 / aerospace8030088` (cit. on p. 5).

[5] Alessandro Zavoli. «Indirect Optimization of Bang-Bang Control Problems and Applications to Formation Flying Missions». PhD thesis. Torino: Sapienza, Università di Roma, May 2013. URL: `https://iris.uniroma1.it/retrieve/ e3835315 - d387 - 15e8 - e053 - a505fe0a3de9 / Alessandro%20Zavoli%20 - %20PhD%20thesis%20-%20Ciclo%20XXV%20-%20padis.pdf` (cit. on pp. 5, 13).

[6] Yu-Chi Ho Arthur E. Bryson Jr. *Applied Optimal Control*. 1025 Vermont Ave. N.W., Washington, D.C. 20005: Hemisphere Publishing Corporation, 1975 (cit. on p. 6).

[7] Jànos D. Pintér Giorgio Fasano. *Modeling and Optimization in Space Engineering*. Springer New York Heidelberg Dordrecht London: Springer, 2013 (cit. on p. 7).

[8]   L.S. Pontryagin. *The mathematocal theory of optimal processes, International series of monographs in pure and applied mathematics Pergamon Press book.* Pergamon Press; [distributed in the Western Hemisphere by Macmillan, New York], 1964 (cit. on p. 10).

[9]   Jànos D. Pintér Giorgio Fasano. *Space Engineering - Modeling and Optimization with Case Studies.* Springer New York Heidelberg Dordrecht London: Springer, 2016 (cit. on p. 16).

[10] David A. Vallado. *Fundamentals of Astrodynamics and Applications.* Hawthorne, CA: Microcosm Press, 2013 (cit. on pp. 26, 29–33, 36).

[11] Simon A. Holmes Nikolaos K. Pavlis. «The Development and Evaluation of the Earth Gravitational Model 2008 (EGM2008)». In: *Journal of Geophysicl Research* 117 (Apr. 2012). DOI: `10.1029/2011JB008916` (cit. on p. 30).

[12] D. P. Drob J. M. Picone A. E. Hedin. «NRLMSISE-00 empirical model of the atmosphere: Statistical comparisons and scientific issues». In: *Journal of Geophysicl Research* 107 (Dec. 2002). DOI: `10.1029/2002JA009430` (cit. on p. 32).

[13] Eric W. Weisstein. *Circle-Circle Intersection.* Wolfram MathWorld. URL: `https://mathworld.wolfram.com/Circle-CircleIntersection.html` (cit. on p. 34).

[14] Giorgio Pesenti. «Optimization of interplanetary transfers with flybys and deep-space maneuvers». MA thesis. Torino: Politecnico di Torino, 2024 (cit. on p. 34).

[15] T.S. Kelso. *Socrates Plus - Satellite Orbital Conjunction Reports Assessing Threatening Encounters in Space.* CelesTrak. June 2024. URL: `https://celestrak.org/SOCRATES/` (cit. on p. 36).

[16] S. Alfano. «Relating Position Uncertainty to Maximum Conjunction Probability». In: *Journal of the Astronautical Sciences* 53 (2005). URL: `https://link.springer.com/article/10.1007/BF03546350` (cit. on p. 39).

[17] V. Braun K. Merz B. Bastida Virgili. «Current Collision Avoidance service by ESA's Space Debris Office». In: (June 2017) (cit. on p. 41).

[18] P. Lu B. Pan Z. Chen. «Reduced Transversality Conditions in Optimal Space Trajectories». In: *Journal of guidance, control, and dynamics* 36 (Sept. 2013). DOI: `10.2514/1.60181` (cit. on p. 47).